Predictions of high-frequency ground-motion in Taiwan based on weak motion data

Sebastiano D'Amico,[1] Aybige Akinci[2] and Luca Malagnini[2]

[1]*Physics Department, University of Malta, Msida* MSD 2080, *Malta. E-mail: sebdamico@gmail.com*
[2]*Istituto Nazionale di Geofisica e Vulcanologia, via di Vigna Murata 605, 00143, Rome, Italy*

SUMMARY

Following a recent paper we use weak-motion waveforms to calibrate a model for the prediction of earthquake-induced ground-motion in Taiwan, in the 0.25–5.0 Hz frequency range, valid up to M_w 7.6. The excitation/attenuation model is given in terms of frequency-dependent seismic wave attenuation, $Q_s(f)$, geometrical spreading, $g(r)$, a magnitude-dependent stress parameters $\Delta\sigma$ for the excitation terms, and a site term for each seismic station used in the study. A set of weak-motion data was gathered from about 170 aftershocks of the Chi–Chi earthquake, M_w 7.6, of 1999 September 20, (17:47 UTC), recorded by 10 broad-band seismic stations. The moment magnitudes of the registered aftershocks ranged from M_w 3.0 to 6.5, and the hypocentral distances from a few kilometres to about 250 km. A frequency-dependent crustal quality factor, $Q(f) = 350f^{0.32}$, was obtained, to be coupled with the geometrical spreading function

$$g(r) = \begin{cases} r^{-1.2} & 1 < r < 10\,\text{km} \\ r^{-0.7} & 10 < r < 40\,\text{km} \\ r^{-1.0} & 40 < r < 80\,\text{km} \\ r^{-0.5} & r > 80\,\text{km.} \end{cases}$$

Earthquake-related excitation spectra were calibrated over our empirical results by using a magnitude-dependent Brune model with a stress drop value of $\Delta\sigma = 8.0 \pm 1.0$ MPa for the largest event of M_w 6.5 in our data set and with a near surface attenuation parameter of $\kappa = 0.05$ s.

Results on region-specific crustal attenuation and source scaling were used to generate stochastic simulations both for point-source and extended-fault ruptures through the computer codes: Stochastic Model SIMulation, SMSIM and Extended-Fault Model Simulation, EXSIM. The absolute peak ground accelerations (PGA), peak ground velocities (PGV) and 5 per cent-damped Spectral Accelerations (SA) at three different frequencies, 0.33 Hz, 1.0 Hz and 3.0 Hz for several magnitudes and distance ranges were predicted at large magnitudes, well beyond magnitude M_w 6.5, the upper limit for the events of our weak-motion data set. The performance of the stochastic model was then tested against the strong-motion data recorded during the M_w 7.6 Chi–Chi earthquake, and against several other empirical ground-motion models.

Key words: Earthquake ground motion; Seismic attenuation; Asia.

1 INTRODUCTION

The M_w 7.6 Chi–Chi earthquake of 1999 September 20 (17:47 UTC) was the largest event on land affecting Taiwan during the last 100 yr. This earthquake produced devastating effects throughout the region: about 6800 buildings were destroyed, and thousands of people were killed (Tsai *et al.* 2001; Sokolov *et al.* 2004). Along the surface expression of the Chelungpu Fault, the Chi–Chi earthquake produced a surface rupture of about 100 km (Huang *et al.* 1999). A large volume of high quality data had been recorded during the event, offering an excellent opportunity to investigate many fundamental issues related to the seismic sequence (e.g. D'Amico *et al.* 2010), complex source rupture, crustal wave propagation, as well as to calibrate tools for the prediction of strong ground motion.

The distribution of ground motion parameters, Peak Ground Acceleration (PGA) and Peak Ground Velocities (PGV) were analysed in several studies as a function of distance and frequency (Chang *et al.* 2000; Wang *et al.* 2000; Sokolov *et al.* 2002; Roumelioti & Beresnev 2003). Although the strong ground motion records during the Chi–Chi earthquake showed various characteristics at different sites in Taiwan, its high-frequency ground-motion levels in terms of PGA were between 0.5 and 0.7 times the worldwide average for soil and rock sites, respectively. Unlike the horizontal PGA, the observed horizontal PGV values are relatively high when compared with predictions for an earthquake of the same magnitude by an existing Ground Motion Predictive Equation (GMPE) based on a set of worldwide data (Tsai & Huang 2000).

Quantifying the crustal wave propagation in the region, together with the earthquake source and site properties, is crucial for predicting future earthquake-induced ground motion. At present, several studies demonstrate that the ground motions are different for different seismic regions (Malagnini & Herrmann 2000, Malagnini *et al.* 2000a,b, 2002, 2004a, 2007, 2008, 2011; Akinci *et al.* 2001, 2006, 2010; Cotton *et al* 2008; Drouet *et al.* 2008, 2010; Edwards *et al.* 2008; Atkinson & Morrison 2009), so that region-specific ground motion models should be developed. As first suggested by Chouet & Tsujiurs (1978), and described in detail by Malagnini *et al.* (2007), the crustal attenuation properties at high frequencies, as well as the site specific effects can be evaluated by studying moderate and small size earthquakes. A complete description for the characteristics of regional ground motion attenuation can easily be calibrated from the regional seismic networks, and can be used as a basis for including large earthquake data.

Although the attenuation and site terms can be established regionally from data of smaller events, or even in absolute terms (Malagnini *et al.* 2004b), the source stress parameter (i.e. the Brune stress drop) extracted from such a data set might be inadequate for the larger events. Consequently, the debate may be shifted from whether these predictions can be used in the case of larger events, to how to extend them to magnitudes larger than those of the events on which the model calibration is carried out. The knowledge of source scaling is fundamental to seismic hazard prediction, earthquake rupture simulations and seismic discrimination, especially if the variation of the apparent stress is magnitude and/or region-dependent (Mayeda & Malagnini 2009). Therefore, it becomes important to understand whether the earthquake source scaling is self-similar or not, and, consequently, to quantify the stress parameter as a function of magnitude. In fact, Mayeda & Malagnini (2009) hypothesized that the source scaling is self-similar (i.e. earthquakes are characterized by constant stress drop) only above and below M_w 5.5. The abrupt jump in stress parameter observed at M_w 5.5 can then be related to dynamic lubrication mechanisms of the fault (Malagnini & Mayeda 2008; Malagnini *et al.* 2010a).

In this study, we characterize the scaling of high-frequency ground-motion based on weak-motion data in Taiwan. The used regression technique has been successfully applied in many regions all over the world such as California (Raoof *et al.* 1999, Malagnini *et al.* 2007), Turkey (Akinci *et al.* 2001, 2006), Italy (Malagnini & Herrmann 2000; Malagnini *et al.* 2000a, 2002; Scognamiglio *et al.* 2005; Morasca *et al.* 2006), Mexico (Ortega *et al.* 2003), India (Bodin *et al.* 2004), central Europe (Bay *et al.* 2003; Malagnini *et al* 2000b). Such studies clearly demonstrate that the weak-motion based ground-motion predictive equations can successfully be used to quantify the ground motions induced by larger events, once the source term is adequately calibrated (Malagnini *et al.* 2011). Intermediate-to-high frequencies are sensitive to changes in the stress parameter. Then the choice of the stress parameter to be used in the source term of our ground-motion model for magnitudes higher than M_w 6.5 is crucial in our study because this is the largest magnitude of event in our weak-motion data set. Therefore, we used a Brune like stress parameters as suggested by Mayeda & Malagnini (2009): $\Delta\sigma = 9.0$ MPa at M_w 7.6 and $\Delta\sigma = 8.0$ MPa corresponding to M_w 6.5 which the latter is agree with our excitation term results. For the main shock and the three larger aftershocks of the Chi–Chi sequence, these authors calculated stress parameters clustered around 9.0 MPa, independently from the regressions on the regional wave propagation, from moment-rate spectra using the coda method of Mayeda *et al.* (2003). These stress parameters fit to our source excitation terms very well at M_w 6.5 and below.

Finally, to test the performance of our region-specific ground motion model, we predicted strong ground motion parameters for moderate-to-large magnitude events as a function of frequency and distance and compared these with the observed accelerations data of 1999 Chi–Chi sequence. To obtain results of general significance, we decided to use selected site responses taken from the NEHRP site classifications (Building Seismic Safety Council, BSSC 2001), like generic rock ($V_{s30} = 620$ m s^{-1}), and generic soil site ($V_{s30} = 310$ m s^{-1}) as classified by Lee & Tsai (2008) and Kuo *et al.* (2011) for the strong motion network in Taiwan. Ground motion predictions have been performed through two widely used stochastic point-source and finite-fault simulation computer codes; SMSIM and EXSIM (Motazedian & Atkinson 2005; Assatourians & Atkinson 2007; Boore 2009), respectively. These simulations allow us to extrapolate predictions for magnitudes larger than those sampled in the data set (M_w 3.0–6.5 in our case). For example; the M_w 7.6 Chi–Chi earthquake was not a part of the database used in the predictive study and we used it as a validation test for the extrapolation of predictions to more than one magnitude unit above the largest event of the calibration data set. We showed that a stochastic model based on region-specific attenuation and source parameters determined provides an excellent fit to the observed data recorded during the main shock, up to about 200 km of Joyner-Boore distance.

2 SEISMOTECTONIC SETTING

The size of Taiwan is quite small, approximately 400 km by 200 km, although it occupies one of the most seismically active and complex regions of the planet, where the Philippine Sea and Eurasian Plates collide (Fig. 1). Taiwan is the accretionary prism built from this collision (Ho 1986; Liu *et al.* 1997) in the past 5 million years (Teng 1990). Yu *et al.* (1997) first estimated the present day crustal motion for the Taiwan area using GPS data. Yu *et al.* (1999) reported that the Chinese continental margin moves at a rate of about 12 mm yr^{-1} in the east-southeast direction and the Luzon arc moves at a rate of about 70 mm yr^{-1} in the northwest direction relative to the stable part of the Eurasian Plate. This ongoing collision is the cause of the high seismicity rate, and the large earthquakes in the region. The Taiwan mountain belt is considered to be the result of the late Cenozoic convergence between these two plates (Ding *et al.* 2001), and this region appears as one of the most unstable areas of the world, with frequent major earthquakes.

3 WEAK-MOTION DATA SET AND DATA PROCESSING

A regression analysis was performed in this study on a weak-motion data set of waveforms from 170 earthquakes recorded by the
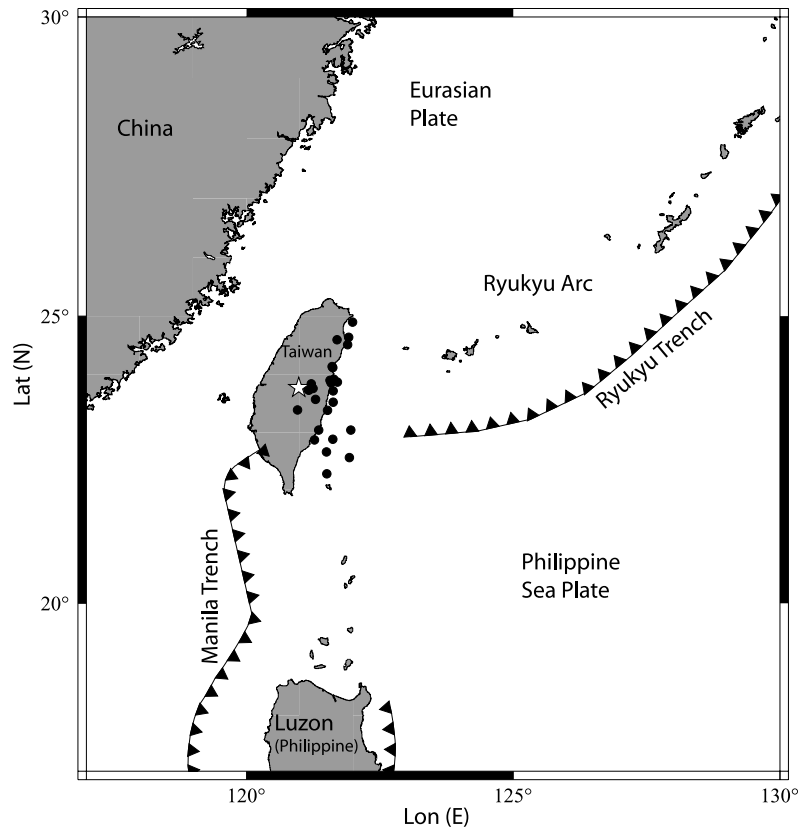
Figure 1. Simple structural map of the Taiwan area. Earthquakes with magnitude greater than 6 from 1980 reported by the NEIC–USGS catalogue (http://neic.usgs.gov/neis/epic) are also shown. The star represents the 1999 September 20, Chi–Chi earthquake.

Broad-band Array in Taiwan for Seismology (BATS) seismic network, which is run by the Institute of Earth Sciences, Academia Sinica, Taiwan (Fig. 2a). The stations are equipped with broad-band sensors (Streckeisen STS-1 or STS-2) and 24-bit digital recorders (Quanterra Q-680 or Q-4120). We mainly used recordings from the aftershock sequence that followed the M_w 7.6 Chi–Chi earthquake, with moment magnitudes ranging from 4.0 to 6.5. The characteristics of our data set are reported in Figs 2(b) and (c).

Following the approach described Malagnini *et al.* (2000a, 2007) we processed a large number of weak-motion data. No hypothesis on the functional form of the scaling laws needs to be formulated before the analysis. The method takes into account the duration parameter, as a function of frequency and distance, through the statistical tool called Random Vibration Theory (RVT, Cartwright & Longuet-Higgins 1956). The latter is used to estimate the peak ground motion of a random time history, given the empirical attenuation parameter, source spectrum and its duration in time. A detailed description of the method and data processing technique are provided in Malagnini *et al.* (2000a, 2007).

Each waveform was visually inspected to eliminate recordings with low signal-to-noise ratios, anomalous glitches and calibration issues. Every seismogram was also corrected for the instrument response, and translated to ground velocity in metres per seconds. The pickings of the *P*- and *S*-wave arrivals were also reviewed. Each corrected time-series was filtered around nine different central frequencies ($f_c = 0.25, 0.4, 0.6, 0.85, 1.25, 1.75, 2.5, 3.5, 5.0$ Hz), using bandpass filter at every f_c constructed as the contribution of two 8-pole Butterworth filters: a low-pass filter and a high-pass filter with corner frequency, respectively, at $\sqrt{2}f_c$ and $1/\sqrt{2}f_c$.

A general form for a predictive relationship for observed ground motion is

$$A_{ij}\left(f, r_{ij}\right) = EXC_i\left(r_{\text{ref}}, f\right) + \text{SITE}_j\left(f\right) + D\left(r_{ij}, r_{\text{ref}}, f\right), \quad (1)$$

where $A_{ij}(f)$ represents the logarithm of observed peak amplitude of ground-motion velocity at site '*j*' for the earthquake '*i*' on each filtered seismogram recorded at the hypocentral distance r_{ij}, $EXC_i(r_{ref}, f)$ is the excitation term (level of the signal from reference distance, (r_{ref}); $\text{SITE}_j(f)$ represents the site term and describes the site modification effects; and $D(r_{ij}, r_{\text{ref}}, f)$ is the crustal propagation term and represents an estimate of the average frequency-dependent crustal response for the region, propagates the signal from the reference distance to the distance of observation. By using the eq. (1), we can arrange all our observations in a large matrix and then invert to obtain source, path and site terms. Although eq. (1) is simple in appearance, the true separation of these terms is difficult to achieve because of hidden trade-offs. For example, special care must be taken to select recording sites at a large range of hypocentral distances, so that undesirable trade-offs between an event source term and the distance function are avoided. Constraints must also be applied to reduce the number of degrees of freedom of the system, and to permit a stable inversion as following

$$D(r_{ij} = r, r_{\text{ref}}, f) = 0 \quad (2a)$$

$$\sum \text{SITE}_i(f) = 0 \quad (2b)$$

The first constraint in eq. (2) defines the distance to which the excitation term is projected and the propagation term is normalized
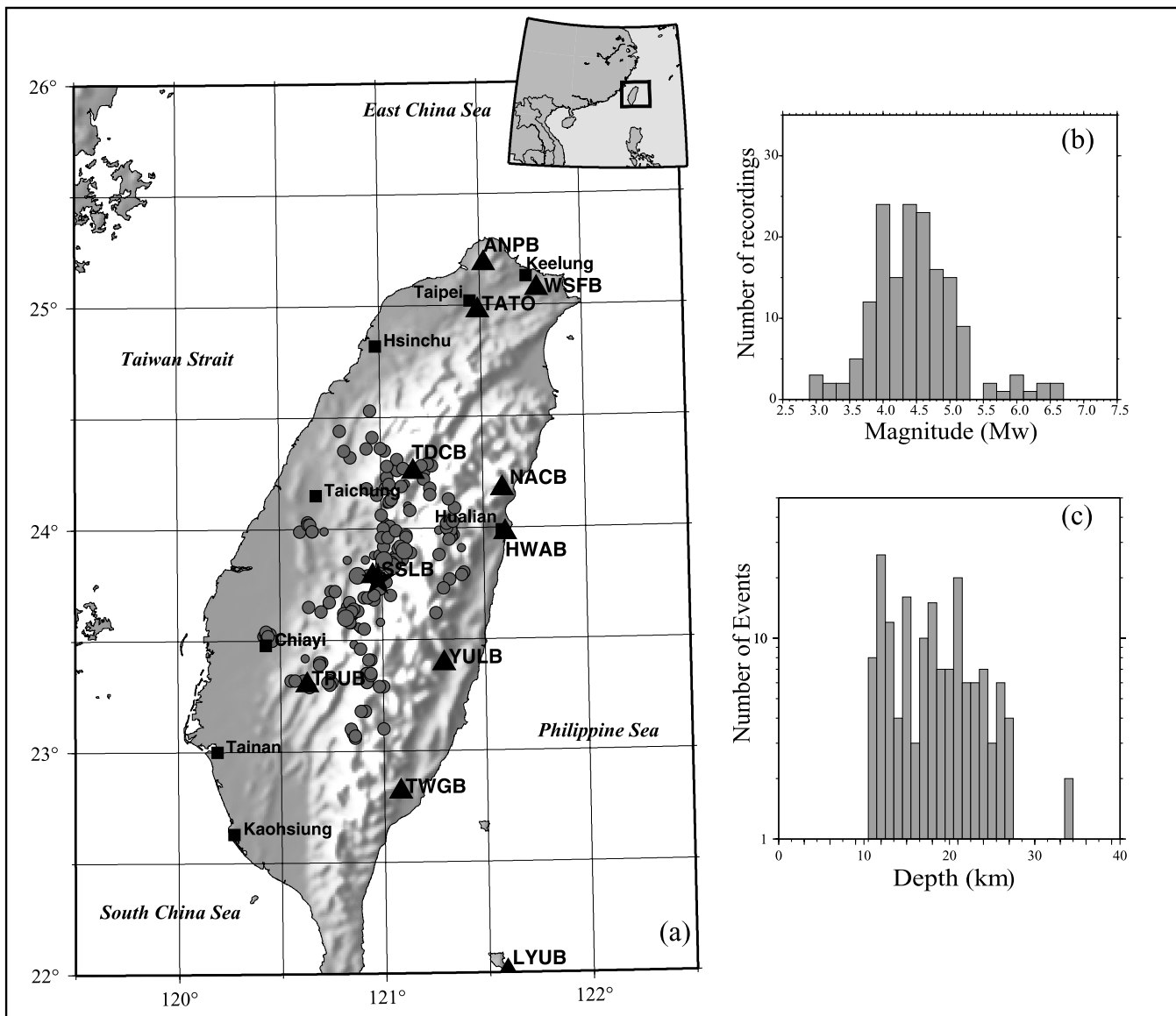
Figure 2. (a) Map of the region showing the events used for the regression (circles) and the seismic stations used in this study (grey triangles). Characteristic of our data set are also shown, the right panels report the distribution of the events as a function of moment magnitude (b) and the distribution of the events as a function of depth (c).

to this arbitrary reference distance. In this study, we choose $r_{ref} = 40$ km. The value of r_{ref} is chosen to be within the range of observed distances, large enough so that errors in the focal depth do not make a major difference in the hypocentral distance, but smaller than the distance where the first supercritical reflections from crustal interfaces appear. A piece-wise linear function defined by fixed-distance nodes was used to model the $D(r;r_{ref},f)$ function. The number of nodes of this piece-wise linear function, and the spacing between the nodes are selected according to the distance distribution of our data. The effect of the second one in eq. (2) is that common site effects are mapped on the excitation term. During the inversion the sum of all site terms is forced to zero (relation 2b) for each frequency, so that the source terms represent what would be recorded at the reference hypocentral distance by the average network site. Each individual site term measures the deviation from the mean seismic spectra for each station, which is due to the physical properties of the shallow geology at the recording site or, in some cases, to instrumental calibration.

4 RESULTS

4.1 Duration of the ground motion

The duration of ground motion is, in general, a function of the fault size and of the dispersion of elastic waves along the path between the source and the seismic station. To make specific predictions for large earthquakes, the duration of the event must be added in the form of a constant term equal to the inverse of the corner frequency. Because no unique definition of the effective duration of the ground motion is possible, we define the effective duration for the ground motion as it is given by Raoof *et al.* (1999). Then for each seismogram the duration T is determined as the width of the time window that delimits the 5–75 per cent portion of the seismic energy following the *S*-wave arrivals. Fig. 3 shows the duration for all the available records.

In what follows, peak ground motions (PGA and PGV) are predicted by using the 2.5-Hz duration function, which was chosen to
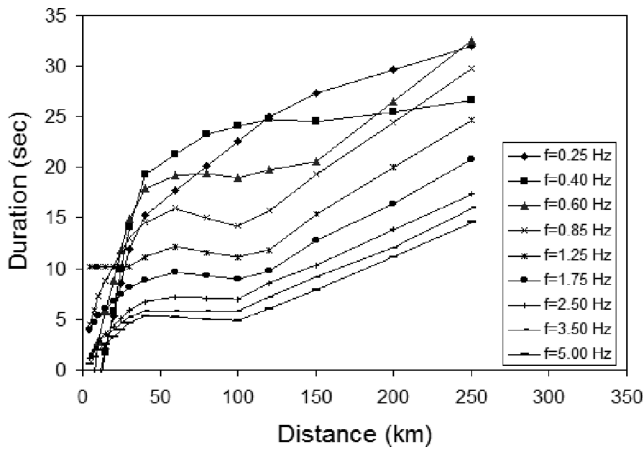
Figure 3. Duration of the seismic signal as a function of hypocentral distance for each frequency studied.

reach an acceptable compromise, because PGAs and PGVs are carried, at different distances, by wavetrains with different dominant frequencies.

4.2 High-frequency crustal attenuation and geometrical spreading

The functional form for the propagation terms expresses the effects of frequency-dependent geometrical spreading and anelastic attenuation (Aki 1980), depending, for each frequency, on the average velocity structure along the propagation path and rock's physical properties. Therefore, we obtain the results of the regression at a set of sampling frequencies, and model them by using the following

functional form

$$D(r, r_{ref}, f) = \log[g(r)] - \log[g(r_{ref})] - \frac{\pi f (r - r_{ref}) \log e}{\beta Q(f)}, \quad (3)$$

where $g(r)$ is the apparent geometrical spreading, β is the shear wave velocity and the frequency-dependent attenuation is defined through the quality factor, $Q(f)$, which is defined as

$$Q(f) = Q_0 \left(\frac{f}{f_{ref}}\right)^{\eta} \quad (4)$$

with the reference frequency f_{ref} chosen at 1 Hz. The parameter η defines the frequency dependence of $Q(f)$.

The term: $\log_{10}(D(r, r_{ref}, f))$ is modelled as a piecewise linear function between a number of distance nodes, and assumed to be zero at a reference distance r_{ref}, which defines the excitation term $\log_{10}(EXC_i(r_{ref}, f))$. The r_{ref} is chosen such that mislocations in source depth would not significantly change the reference hypocentral distance. The coloured curves in Fig. 4 represent the empirical regional attenuation terms for the peak filtered amplitudes. The black lines in the background represent the frequency dependent synthetic RVT predictions of the empirical $D(r, r_{ref}, f)$ function, normalized to zero at the arbitrary reference hypocentral distance of 40 km. For these predictions, we used the attenuation model having $Q_0 = 350$, $\eta = 0.32$ at $f_{ref} = 1.0$ Hz

$$Q(f) = 350(f)^{0.32} \quad (5)$$

and used all the frequency-specific estimates of duration presented in Fig. 3. A body-wave like geometric attenuation is used to model the decay of the Fourier amplitudes at distances up to 80 km like decay, ($g(r) = r^{-1.0}$; all frequencies), and a surface-wave like decay,
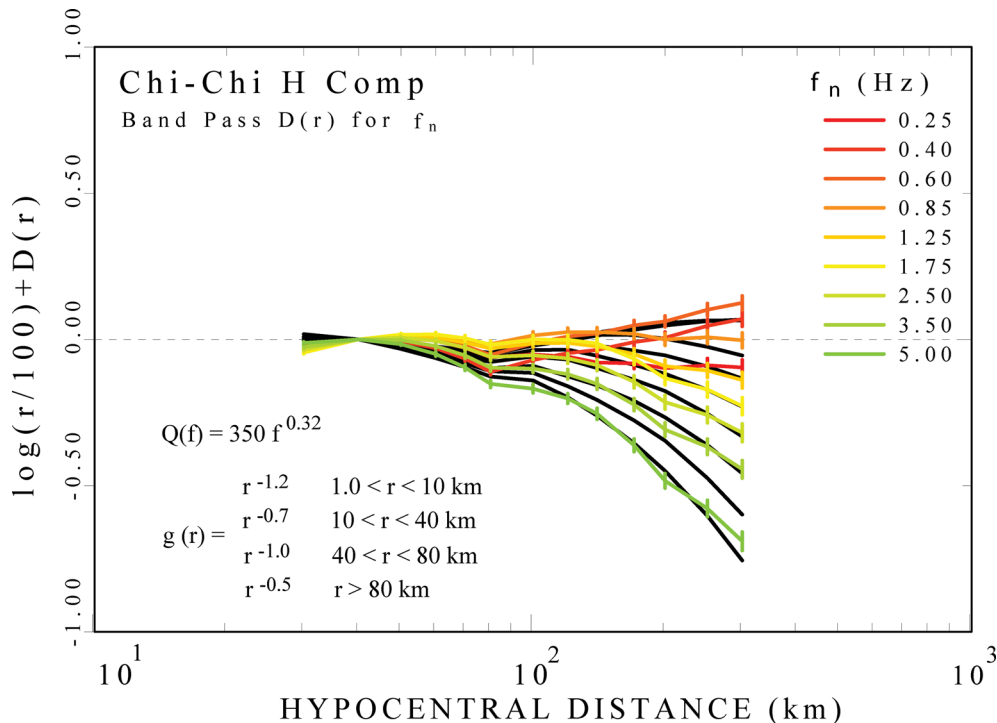
Figure 4. Coloured curves represent the empirical propagation term, at different central frequencies, resulting from the regression of the peak value of the data set waveforms. Black solid lines are the theoretical prediction. The attenuation term was forced to zero at the reference distance of 40 km.

$(g(r) = r^{-0.5})$, fits the results at larger hypocentral distances.

$$g(r) = \begin{cases} r^{-1.2} & 1 < r < 10 \, \text{km} \\ r^{-0.7} & 10 < r < 40 \, \text{km} \\ r^{-1.0} & 40 < r < 80 \, \text{km} \\ r^{-0.5} & r > 80 \, \text{km} \end{cases} \tag{6}$$

4.3 Excitation terms

The source excitation, $\text{EXC}_i(r_{\text{ref}}, f)$ in eq. (1), may be thought of as the average expected level of ground motion at r_{ref} for each earthquake. The observed excitation is related to the actual source spectrum through the expression

$$10^{\text{EXC}i(r,\text{ref},f)} = s(f, M_{\text{w}}) \, g(r_{\text{ref}}) \exp[-\pi f r_{\text{ref}}/Q(f)\beta]$$
$$\{V(f)\exp(-\pi f k_{\text{o}})\}_{\text{avg}}, \tag{7}$$

where $s(f, M_{\text{w}})$ is the source excitation as a function of moment magnitude, $V(f)$ is a frequency-dependent 'regional' site amplification (the average site term of the stations included into eq. 2(b) and κ_0 controls near-surface attenuation at high frequency. The term $[g(r_{\text{ref}}) \exp(-\pi f r /Q(f)\beta)]$ represents the effect of the propagation at the reference distance due to geometrical spreading and crustal attenuation. The term $\{V(f)\exp(-\pi f \kappa_0)\}_{\text{avg}}$ term controls the average site modification of the signal spectrum. $V(f)$ represents the average site amplification term relative to hard rock (in the manner of Atkinson & Silva 1997), and can be calculated from the shallow shear wave velocity structure near the site (Boore 1996). κ_0 describes the depletion of the high-frequency motion at the site, which may be caused by the local $Q(z)$ structure. The form of $s(f, M_{\text{w}})$ representing the Fourier velocity spectra is following

$$s(f, M_{\text{w}}) = K \left[M_o/4\pi\rho\beta^3 \right] (2\pi f) S(f), \tag{8}$$

where $\log M_o = 1.5(M_{\text{w}} + 6.03)$ (M_0 in Nm; from Hanks & Kanamori 1979), $K = (0.55 \times 2.0 \times 0.707)$ is a coefficient composed of the effects of the average radiation pattern, free-surface amplifications for vertically incident S waves and the energy partition of initial shear wave amplitude into two horizontal components, M_o is the seismic moment, ρ is the mass density at the source and β is the shear wave velocity at the source. $S(f)$ is the single-corner source term

$$S(f) = 1/\left[1 + (f/f_c)^2 \right], \tag{9}$$

where $f_c = 0.49\beta(\Delta\sigma/M_o)^{1/3}$. Here the corner frequency f_c is determined from the spectra and is related to the stress drop, $\Delta\sigma$ (Pa), seismic moment, M_o (Nm) and the shear wave velocity β (m s^{-1}). The constant 0.49 depends on the type of model spectra and the geometry of the source.

To model the excitation term, we use Brune's (1970, 1971) ω^2 source model, which describes the spectrum of shear radiation in terms of stress drop and moment magnitude. Fig. 5 shows the empirical/inverted excitation terms (black colour, thin lines) obtained through the regressions of the filtered peak amplitudes, for which RVT was used. The empirical terms are superimposed to the theoretical/synthetic excitation terms (grey colour, thick line) at various magnitudes. Synthetic lines were obtained by combining the Brune spectral model, the regional geometric/anelastic attenuation just defined for the regional propagation terms, and the assumed site responses taken from the Boore & Joyner (1997) for generic rock site condition ($V_{s30} = 620$ m s^{-1}) with the network-averaged attenuation parameter of kappa, κ 0.05 s. Our estimate of the high frequency cut-off parameter, κ is 0.05 s (Anderson & Hough 1984);
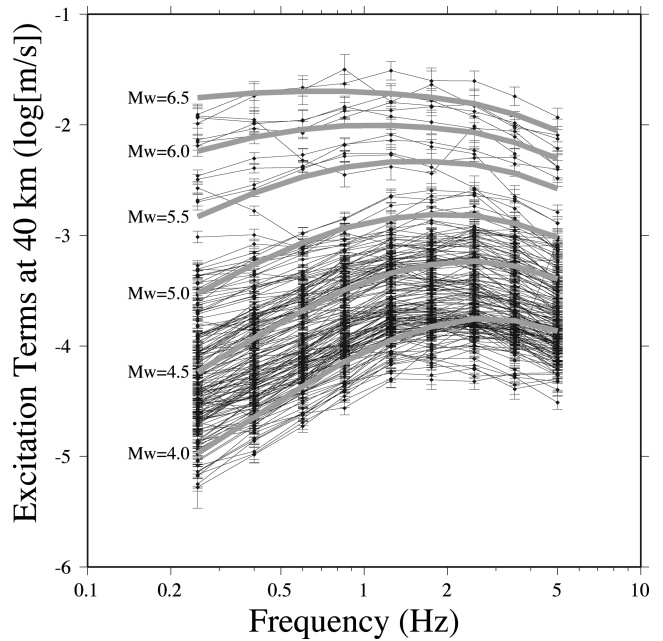
Figure 5. Excitation of peak filtered velocity at a reference hypocentral distance $r_{\text{ref}} = 40$ km. Excitation terms for all events used in this study with magnitude between $M_{\text{w}} = 4.0$ and 6.5 are compared to predictions obtained by using RVT. The grey curves representing the theoretical source terms are computed for magnitudes of 4.0, 4.5, 5.0, 5.5, 6.0 and 6.5 by using the parameters of Table 1.

was estimated by performing a best fit of the spectra of an average spectral shape using small earthquakes of magnitude.

We adjusted the average stress parameter required to best reproduce the observed propagation-corrected source spectra for the larger earthquakes in our data. Although this method is not very flexible, it yields an average, single-corner frequency model with stress drop of about 8.0 MPa, which is completely in agreement with the value calculated at M_{w} 6.5 by Mayeda & Malagnini (2009).

In fact Mayeda & Malagnini (2009) calculated the stress parameters from absolute source spectra applying a spectral ratio technique (Mayeda *et al.* 2007) for the M_{w} 7.6 Chi–Chi earthquake and about 20 of its aftershocks. The advantages of using spectral ratios are that path and site attenuation correction are not needed since the event pairs have common path and site effects. For the main shock and three of the larger aftershocks, apparent stress is obtained as clustered around 9.0 MPa ($\pm$ 1.0 MPa). Events below $M_{\text{w}} \sim 5.5$ exhibit lower apparent stress with larger scatter, ranging between 0.8 and 8.0 MPa and are spatially variable (Fig. 6). However, in this study we adopted the stress parameters from Mayeda & Malagnini (2009) to perform the ground motion predictions through the stochastic simulations.

5 PREDICTION OF GROUND MOTION PARAMETERS AND COMPARISON OF EMPIRICAL DATA

Using the source scaling defined by Mayeda & Malagnini (2009), and the crustal attenuation developed in this study, we defined a complete spectral model that allows the prediction of the strong ground shaking in Taiwan, that is entirely based on the analysis of a set of weak-motion broad-band waveforms. The Brune's ω-square spectral model, combined with our results on the regional attenuation, and on the duration of the ground motions, were used to
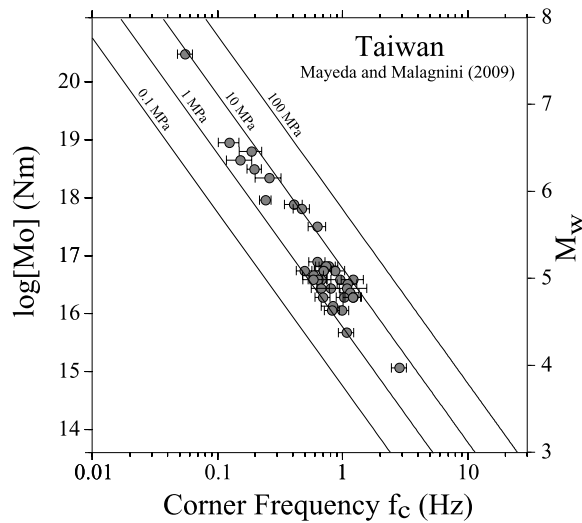
Figure 6. M_o versus fc plot for some of the events of the Chi–Chi seismic sequence. Oblique lines represent constant Brune stress drops (i.e. self-similar distributions). The main shock of the sequence clearly deviates from the self-similar trend of its aftershocks (modified from Mayeda & Malagnini 2009).

compute the ground motion parameters, PGA, PGV and SA, as a function of distance from the source for a range of different moment magnitudes, up to M_w 7.6 (i.e., the Chi–Chi earthquake). Predictions were initially computed based on Boore & Joyner's (1997) generic rock site, using a high-frequency attenuation parameter $\kappa = 0.05$ s, and the generic rock site was convolved with relative transfer functions to NEHRP site classes C ($V_{s30} = 520$ m s^{-1}), and D ($V_{s30} = 270$ m s^{-1}). The necessary parameters for ground motion simulations are given in Table 1.

We used a stochastic approach to simulate strong-ground motions, and to see whether our spectral model is capable of reproducing the strong-motion data recorded during the well-recorded Chi–Chi earthquake (M_w 7.6). We performed the task by using two widely used computer codes; for point-source model, SMSIM and

for extended-source model, EXSIM that is originally developed by Boore (1996, 2003) and Motazedian & Atkinson (2005) and Boore (2009), respectively. During the SMSIM point-source simulations we did not use any information about fault geometry and rupture properties. However, the parameters such as the effects of fault size and orientation, location of the site with respect to the fault, distributed rupture, and rupture heterogeneity that are not included in the stochastic point-source model are important and influence the ground motions from large earthquakes. The effects of an extended source influence not only duration and directivity of the ground motion, but also the shape of the spectra of the seismic waves. To take into account the source complexity, we decided to simulate the ground motion of the M_w 7.6 Chi–Chi earthquake using finite-fault models through the EXSIM computer code. This code was developed by Motezedian & Atkinson in 2005 for earthquake simulations based on dynamic corner frequency using for the stochastic finite-fault modelling. It is an upgraded version of FINSIM (FINite fault SIMulation program), which was developed by Beresnev & Atkinson (1998).

We must stress the fact that the aim of this study is not to produce a path-specific scenario earthquake, but rather to test and to validate our weak-motion based model, and generate averaged motions from a suite of earthquakes. Therefore, what is important to us is to demonstrate that weak-motion data can provide useful information and the empirical parameters such as the seismic wave attenuation, geometrical spreading coefficient and stress drop that can be used in a stochastic simulation to ground-motion predictions (Atkinson & Boore 2006).

5.1 Ground motion predictions based on point-source model, SMSIM

In the following paragraphs, we compare our predicted ground motion parameters, as obtained from the point-source stochastic model, with the observed ground motion parameters of the Chi–Chi earthquake and with several existing GMPEs in the region. The vast strong-motion database collected during the Chi–Chi main shock,

Table 1. Spectral source parameters used for Taiwan Ground-Motion Simulations with EXSIM.

Parameter identification	Parameter value
Fault orientation	Strike = 5°
	Dip = 34°
Fault dimension	For M_w = 7.6: Length = 110 km; Width = 40 km
Number of subsources	21 (strike) × 8 (dip)
Pulsing area	50 per cent
Slip distribution	Ma *et al.* (2001)
Crustal shear wave velocity	3.2 km s^{-1}
Density (crustal)	2.8 g cm^{-3}
Rupture velocity	0.8 × shear wave velocity
Anelastic attenuation, $Q(f)$	$350(f)^{0.32}$
Kappa (s)	0.05 s
Geometrical spreading	$g(r) = \begin{cases} r^{-1.2} & 1 < r < 10\,\text{km} \\ r^{-0.7} & 10 < r < 40\,\text{km} \\ r^{-1.0} & 40 < r < 80\,\text{km} \\ r^{-0.5} & r > 80\,\text{km} \end{cases}$
Windowing function	Saragoni—Hart
Stress drop	M_w = 5.5, $\Delta\sigma$ = 6.0 MPa
	M_w = 6.5, $\Delta\sigma$ = 8.0 MPa
	M_w = 7.6, $\Delta\sigma$ = 9.0 MPa
Amplification factors	Generic rock, generic soil and NEHRP site classifications
Damping factor for PSA	5 per cent
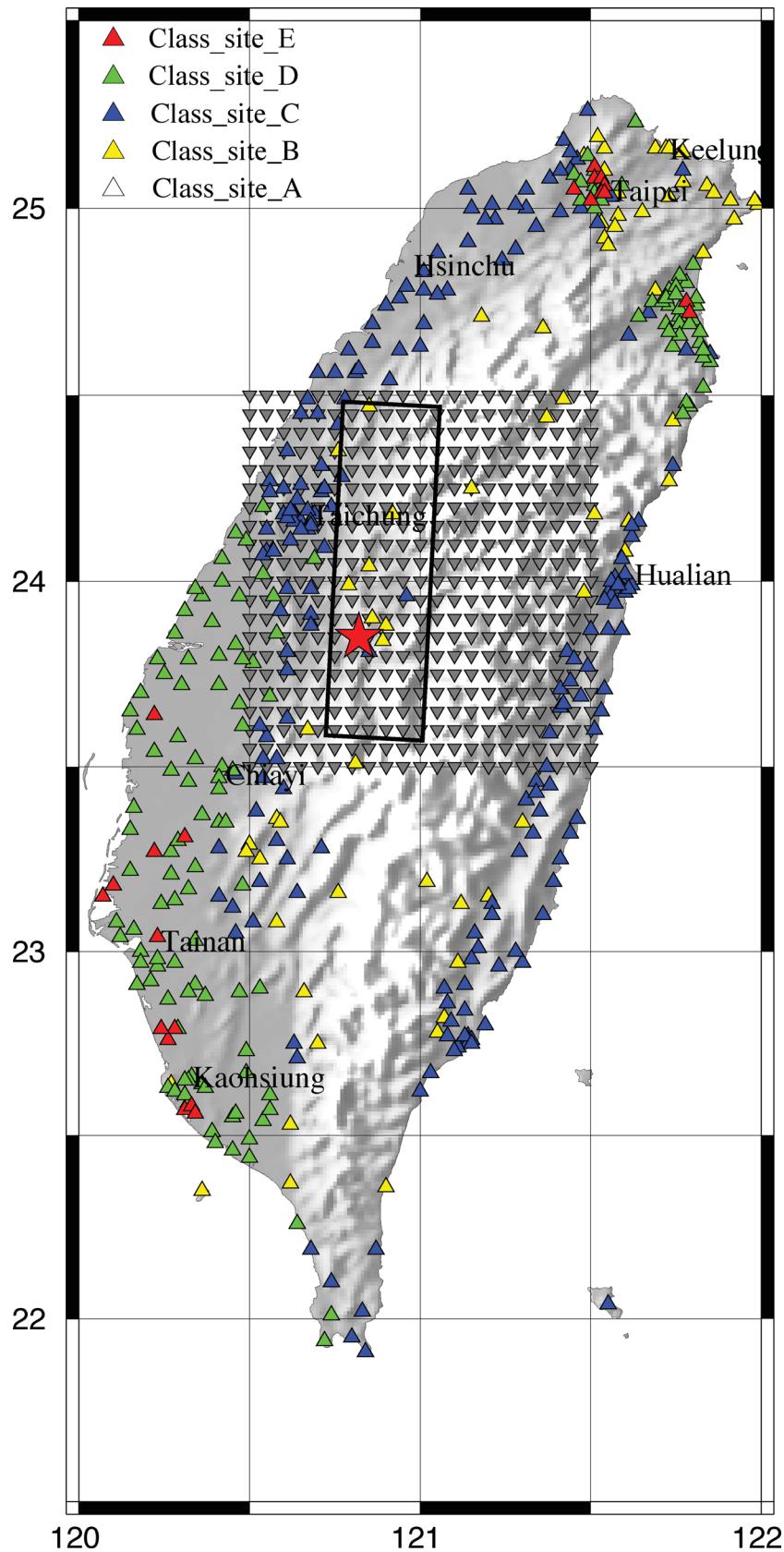
Figure 7. Regional map showing distribution of strong motion instrumentations (TSMIP network) on different geological site conditions where the simulations are calculated using the stochastic finite fault approach. The recording sites have been classified in to NEHRP site classes B, C, D and E as given by Lee & Tsai (2008) and Kuo *et al.* (2011). Inverted triangles indicate the 440 dummy stations around the Chepungpu Fault where the simulations are performed through the finite-fault modelling for generic site condition. The epicentre of the 1999 Chi–Chi earthquake (star) and the surface projection of the fault plane (solid black line) are indicated.

which triggered about 441 instruments, was used for the comparison. The Central Weather Bureau of Taiwan (CWB) provided an extensive strong-motion data set for the main shock and aftershocks of the 1999 Chi–Chi earthquake sequence (Lee *et al.* 2001). This data set is important for both seismological and earthquake engineering research because it includes more than 60 recording sites within 20 km of the fault ruptures and almost complete coverage of the large event of long surface rupture for an M_w 7.6 earthquake. Fig. 7 shows the locations of free-field, three-component strong-motion stations for the recordings on different geologic conditions, and classified into NEHRP site classes B, C, D, and E, according to V_{S30} (Lee & Tsai 2008; Kuo *et al.* 2011). In the strong-motion database, site class B (which included limestone, igneous or metamorphic rocks, hard volcanic deposits and Miocene strata), site class C (very dense soil and soft rocks) are comparable to NEHRP site classes B and C, respectively. Site class D includes fluvial terraces, stiff clays and sandy gravel deposits. Note that most of the stations to the west and to the southwest of the epicentre are located in a deep alluvium of the western coastal plain, as well as the stations located in the Taipei and Ilan Basins north and northeast of the epicentre, that may be on top of sedimentary layers with very low shear wave velocity (Malagnini *et al.* 1997), the importance of which in determining the characteristics of the strong ground motion has been stressed by empirical (e.g. King & Tucker 1984), and numerical studies (e.g. Olsen *et al.* 2006).

Figs 8(a), (b) and 9(a)–(c) show the largest horizontal PGA, peak ground velocity and 0.33Hz, 1.0Hz and 3 Hz, 5 per cent-damped spectral acceleration (SA) recorded for the main shock by the 441 strong motion stations in Taiwan, respectively (displayed with different colours according to their site classifications at each station). The recorded values are compared with our predicted PGA curves for the generic rock and generic soil site classes, plotted as dashed and continuous lines, for M 7.6 events obtained using the point source SMSIM computer code. We also compared the observed and predicted ground motions with the empirical ground motions derived by Akkar & Bommer (2010) (AB10), and two NGA models of Boore & Atkinson (2008) (BA08) and Campbell & Bozorgnia (2008) (CB08) for generic soil conditions, adopting Joyner and Boore distance, R_{jb} as reference measure.

The AB10 derived empirical prediction equations for PGA, PGV and the 5 per cent-damped SA at 18 periods from 0.03 to 2 s, by using a total of 532 strong-motion accelerograms from Europe and the Middle East, recorded at distances of up to 100 km from 131 earthquakes with moment magnitudes ranging from M_w 5.0 to 7.6. The new GMPEs were derived by Boore & Atkinson (BA08), Campbell & Bozorgnia (CB08) in the framework of the Next Generation Attenuation (NGA) project. They used various subsets of a global database of ground motions and metadata from shallow earthquakes in tectonically active regions in the development of the equations (see Chiou *et al.* 2008, for details). The peak acceleration, velocity and displacement, as well as 5 per cent-damped pseudospectral acceleration (PSA) for periods from 0.01 to 10 s were to be valid for magnitudes ranging from 5.0 to 8.5 (for strike-slip faulting) and from 5.0 to 8.0 (for reverse slip faulting), for distances from 0 to 200 km.

In Fig. 8(a), the first observation is the good agreement between observed strong-motion records and our predicted relationships, which includes an anelastic attenuation term up to a distance of 200 km for an event that is more than one unit over the magnitude range covered by the predictive model. The observed PGA values for classes B, C, D and E sites are mixed up, so that we do not observe a clear trend of the data due to the site classification (in the chosen
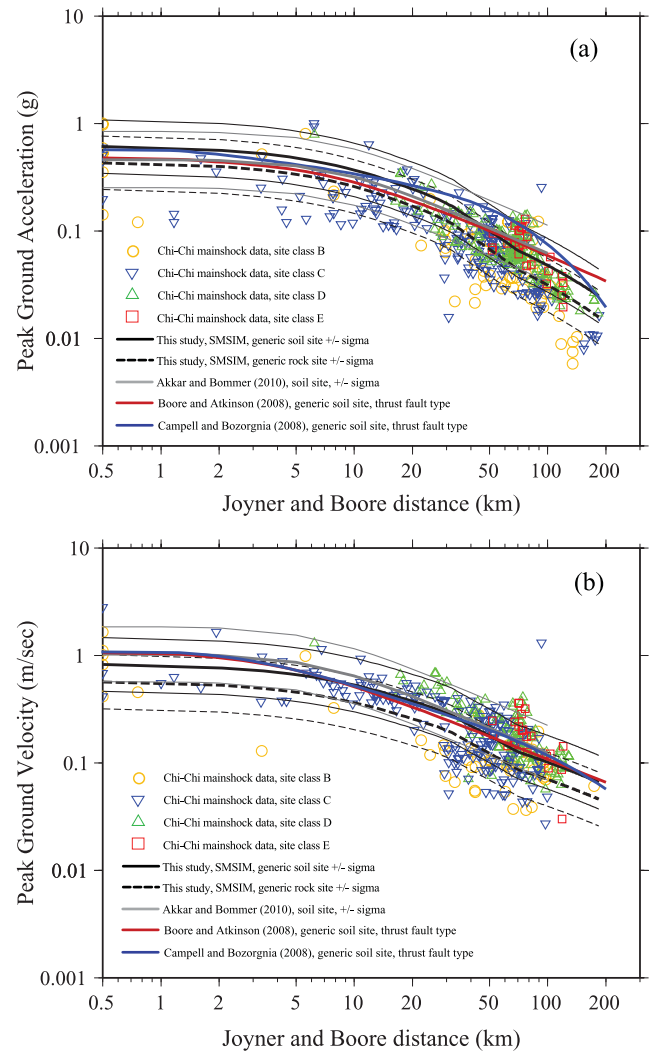
Figure 8 (a) Predictions of PGA for the Chi–Chi main shock (M_w 7.6) and comparison with the observed data. Predictions are calculated through the RVT given the empirical attenuation parameter, source spectrum and its duration in time. Solid and dashed black lines refer to the predictions calculated in this study (median $\pm 1\sigma$) for generic rock and generic soil site classes, respectively, whereas grey lines refer to Akkar & Bommer (2010), and NGA models of Boore & Atkinson (2008), red solid line, and Campbell & Bozorgnia (2008), blue solid line, for generic soil condition. (b) Same as in frame (a) but for PGV. The agreement of the ground motion model presented in this study with the observations gathered during the main shock allows an objective judgment of the model's performance. Observed PGAs and PGVs are characterized by their site classes (symbols in colours).

NEHRP site classes). However, the observed PGA values from the Taipei Basin, and the Ilan Basin, at distances between 50 and 80 km, are significantly higher than the rest of the data set (Loh *et al.* 2000; Tsai & Huang 2000; Wen & Yeh 2001). This was probably due to basin amplification. Because our stochastic simulation approaches are not sensitive to the 2-D and/or 3-D structure, local impedance contrast/gradients, source radiation pattern, etc., we are not able to see all these complex behaviours in the simulated ground motions. Nevertheless, also for the sites classified as 'soft soil', we observe a good fit between the observed PGA's and predictions by AB10, BA08 and CB08. Such agreement gets better in terms of PGV (Fig. 8b), underlying the effect of anelastic attenuation. The site
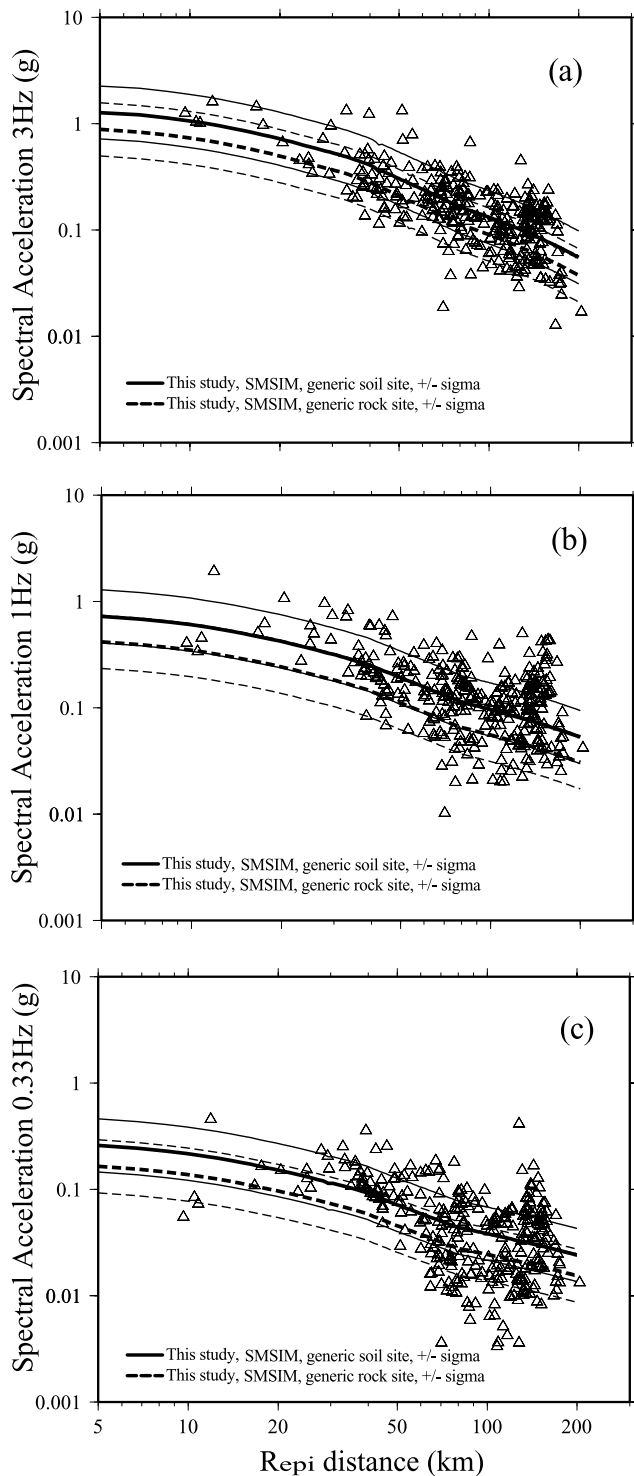
Figure 9. Predictions of SA for the Chi–Chi main shock (M_w 7.6) compared with the observations at three different frequencies (0.33, 1.0, and 3.0 Hz). Frames (a), (b) and (c), corresponding to 3.0 Hz, 1.0 Hz and 0.33 Hz, are used in the ShakeMap® software package, and in Table S1, to provide a complete proof of the validity of the ground motion predictive relationships. The Spectral Acceleration, given in Table S1, was computed using durations at the specific frequencies (0.33, 1.0 and 3.0 Hz).

effects become more evident with respect to PGA, since most of the highest values correspond to stations belonging to class D and E.

Figs 9(a)–(c) present RVT predictions of SA at the three different frequency bands (5 per cent damping) as a function of epicentral

distance, R_{epi}, for generic rock and generic soil site classes, plotted as dashed and continues lines, respectively, for M_w 7.6 event obtained using the point source SMSIM computer code. SA at 3 Hz show a good agreement with the predicted model but exhibit sufficiently larger amplitudes at frequencies 1.0 and 0.33 Hz, (less than 2 Hz). This difference can be caused by the surface wave generated by the Chi–Chi earthquake.

Taking into account the complexity of the examined event and the simplicity of the model, as it is seen in Figs 8(a), (b) and 9(a)–(c), the predictive ground motion model for PGA, PGV and SA spectral parameters fits well the strong-motion data from the Chi–Chi earthquake, well above the maximum magnitude included in the data set. The prediction of ground motion parameters of the PGA and PGV are included in the Supporting Information (Table S1). The SA's predictions (also given in Table S1) were computed using duration at the specific frequencies (0.33 Hz, 1.0 Hz and 3.0 Hz).

5.2 Ground motion predictions based on extended-fault model, EXSIM

The observed variability of the ground motion, observed mainly at near-source distances, is mostly related to the details of the rupture propagation over the fault. The effects of a large finite source can profoundly influence amplitude, frequency content and duration of the ground motion (Beresnev & Atkinson 1997). Therefore, in this section, we reproduce the strong ground motion recordings obtained during 1999 Chi–Chi (M_w 7.6) earthquake by taking into account its source complexity using the stochastic finite fault simulation method based on a dynamic corner frequency approach. The method requires region-specific source, path and site characterizations as input model parameters (Table 1). To define the source mechanism of the earthquake, the finite fault technique requires the specification of the fault geometry including dip and strike angles, depth of the fault, hypocentre location and subfault size. When available, the slip distribution may be another input parameter.

The source mechanism and the rupture processes of the 1999 Chi–Chi event are well constrained from previous studies of the earthquake. This earthquake ruptured about 100 km of the Chelungpu Fault, with a complicated surface faulting (Ma *et al.* 1999). The faulting was mainly a thrust movement on a plane that dipped shallowly (20–30°) to the east. This earthquake produced some of the largest fault displacements (up to 8 m) and largest ground velocities (up to 3 m s^{-1}) observed for a modern earthquake (Chung & Shin 1999).

5.3 Model parameters for EXSIM

In this study, among various models (e.g. Chang *et al.* 2000; Wang *et al.* 2000; Ma *et al.* 2001; Wu *et al.* 2001; Zeng & Chen 2001) we selected source models constructed by Chi *et al.* (2001) and Ma *et al.* (2001) regarding to its fault dimensions and slip distributions on the fault plane, respectively. Ma *et al.* (2001) investigated the rupture process of this earthquake and proposed a single planar fault with a spatiotemporal slip distribution along the fault based on a joint inversion of strong-motion, teleseismic and GPS data from the Chi–Chi event, minimizing the error between the observed and simulated records in particular for the low-frequency content of the Fourier spectra (governed mainly by the source). The results for the simple single fault plane model show a large asperity located in the region about 25–55 km north of the hypocentre with maximum
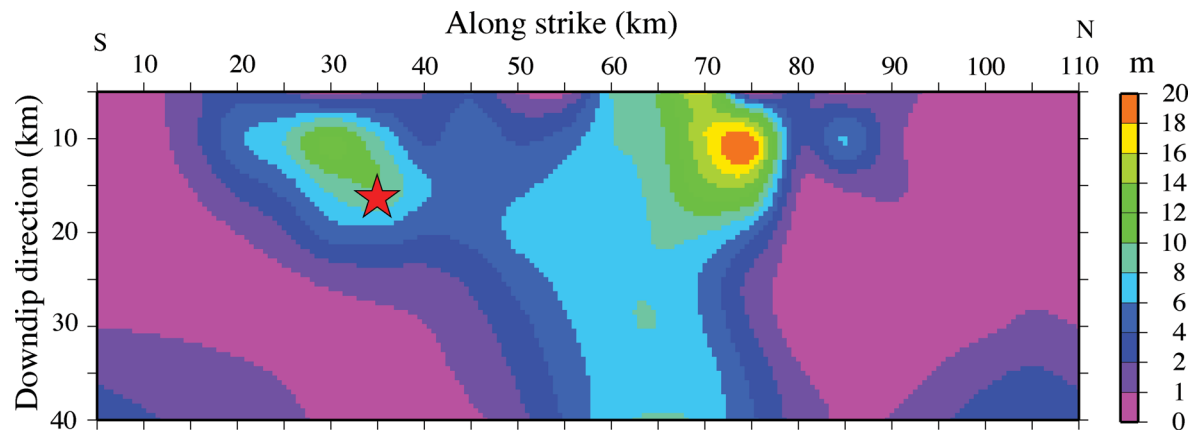
Figure 10. Spatial slip distribution from the combined inversion of strong-motion, teleseismic, and GPS data as given by Ma *et al.* (2001) used for the simulations in this study. The colour bar indicates the amount of slip within the fault plane. The asterisk indicates the hypocentre.

slip of about 15 m (Fig. 10). All other source-related studies for this earthquake consistently show a large asperity in the northern part of the fault. Most of the slip is concentrated at shallow depths (less than 10 km). The rectangular fault with dimensions of 110 km × 40 km and with a strike of 5° and an easterly dip of 34° is used for our simulations. The fault plane was discretized into 21 × 8 subfaults, assigning a subfault dimension of 5 × 5 km and the hypocentre was placed at the south/central upper half of the fault. We assumed that the rupture propagates radially with a constant rupture velocity of 2.8 km s^{-1} (80 per cent of *S*-wave velocity). Fig. 7 shows the surface projection of the adopted fault in this study. In the simulations, the path effects are modelled through geometrical spreading, anelastic attenuation, and ground motion duration parameters obtained in this study. We described the site effects as the combined effects of site amplification and the near-surface attenuation, commonly known as the kappa operator, exp$(-\pi\kappa f)$. California-based generic crustal amplification for rock and soil sites proposed by Boore & Joyner (1997) was applied for the stations. Based on present information about the soil type at the stations, the simulation is performed for generic rock sites, which are equivalent to the NEHRP site classifications.

5.4 Near-field distribution of simulated ground motions

To better capture ground motion variability caused by source complexities, we selected a region of 100 km (east–west) by 110 km (north–south) around the Chelungpu Fault, and divided the region into grids of 0.05°, as indicated by the grey reverse triangles shown in Fig. 7. Consequently, by employing the selected model parameters in EXSIM, we simulated synthetic records for 440 dummy stations for generic rock and generic soil site classification. In Figs 11(a), (b), we examined the distribution of ground motion parameters, predicted PGA's and PGV's, within the selected region for generic rock site, respectively.

The PGA and PGV distributions show that the strongest ground shaking occurred both in the epicentral area and around the locations of the large-slip asperity. In fact, the fault plane contains one asperity with a larger slip located in the northern section of the fault where the single patch with largest ground motion was obtained from the simulation. Most of the near-field stations recorded PGA's near 1 g, consistently with the observed PGA distribution in the area, such as TCU129 (see Fig. 11a). Station TCU129 recorded a peak horizontal acceleration higher than 1 g during the Chi–Chi event, but Wen *et al.*

(2001) demonstrated that the observed large difference in ground motion between TCU129 and nearby stations was due to the effect of the concrete pier on which the instrument was mounted. As a consequence, site TCU129 should not be used in studies of peak acceleration attenuation.

However, large ground velocity and displacement are measured in the northern part of the fault, for example, TCU052 and TCU068, where the largest surface breaks are observed. On the hangingwall, both PGA and PGV are extreme, with some of the records having a PGA of over 1 g (station TCU084, see Fig. 11a). Although the ground shaking was, on the contrary, relatively small on the footwall, long-period surface waves caused serious damage in cities built over the sedimentary plains (Chang *et al.* 2002).

Another notable phenomenon for this earthquake is that the PGV is generally larger in the northern area of the source region. A large PGV extends over most of the northwestern Taiwan (Fig. 11b does not cover this area). This clearly reflects the northward rupture source directivity. Furthermore, some places far from the epicentre, such as the Taipei metropolitan area, Ilan plain and along the Longitudinal Valley, have developed notable ground motion amplifications at low frequencies, which we were not able to reproduce because our approach is not appropriate for capturing the variability of ground motion in those frequency ranges.

5.5 Comparison of synthetic and observed Fourier amplitude spectra

The Fourier Amplitude spectra of the strong motion records in comparison with the synthetics are given in Figs 12(a), (b) at 24 selected stations. Among the selected stations, TCU046, TCU071, TCU079, TCU084, TCU089 and TCU137 are located on the surface projection of the fault plane. Other stations are selected from different locations and orientations respect to fault plane (Fig. 12b). Fig. 12(a) presents the Fourier amplitude spectra at the six selected stations on the fault plane with the simulation results computed using our attenuation and excitation model. The frequency content and the durations of the synthetic ground motions are in close agreement with those of the observations. As observed from the figures, simulations provide reasonable estimates of the general shape and amplitudes of the spectra for most of the stations. These spectra demonstrate the performance of our model very well. Taking into account the complexity of the Chi–Chi event and relatively simpler model used in the study, the fit can be considered very satisfactory.
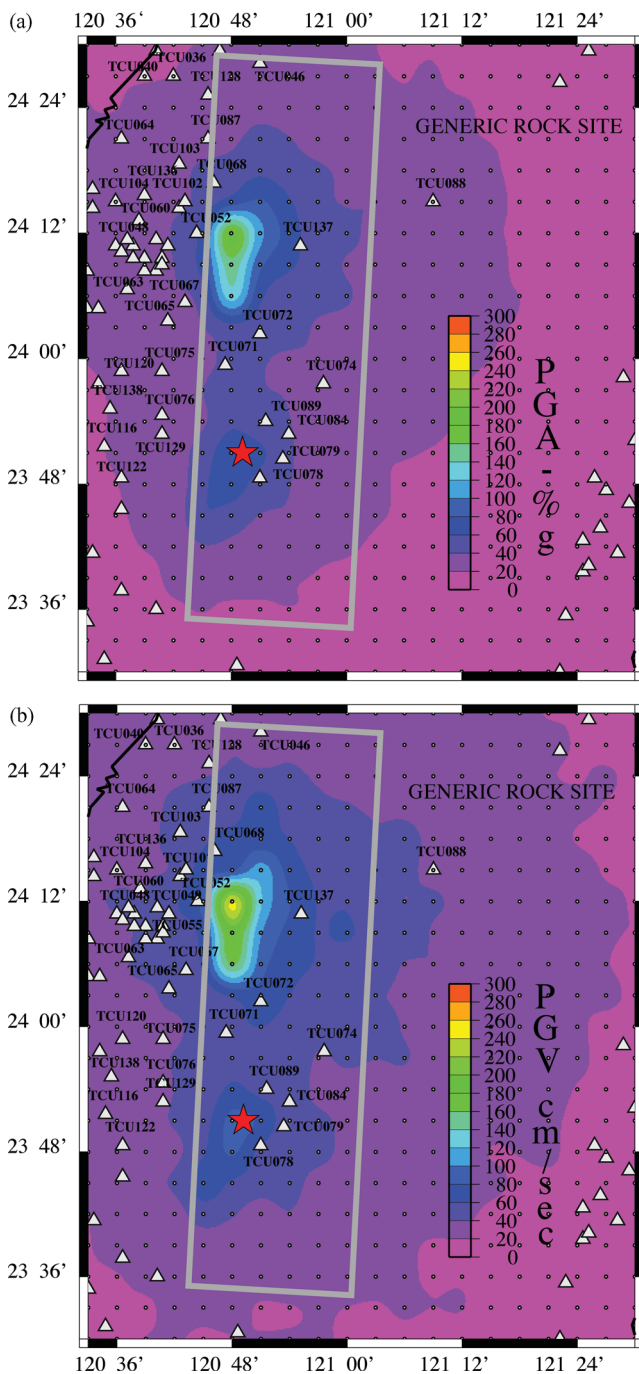
Figure 11. Distribution of (a) simulated PGA (in per cent g) and (b) PGV (in cm s^{-1}) values around the Chelungpu Fault. Dots are the 440 dummy sites that the simulations are calculated taken into account generic rock site condition. The epicentre of the 1999 Chi–Chi earthquake is shown with a star and the surface projection of the fault plane (solid black line) are indicated.

5.6 Comparison of simulated ground motions with observed strong-motion data and the recently developed GMPEs

Finally, to compare the simulated results with recent GMPEs derived based on the strong ground motion data up to larger distances, we simulated synthetic records for the TSMIP network of 441 strong motion stations on different geological conditions, as their site classifications of NEHRP B, C, D and E, given by Lee & Tsai (2008)

and Kuo *et al.* (2011). We employed the NEHRP site classifications and amplifications factors with a kappa factor of 0.05 s, as required by Boore & Joyner (1997). Both the recorded and simulated peak accelerations and velocities at distances up to 200 km from the fault are compared to empirical GMPEs in Figs 13(a), (b). We also merged the simulations performed for generic soil site class at the 440 dummy stations to the simulations calculated for the TSMIP network of 441 strong motion stations on different geological conditions. The three GMPEs shown in Figs 13(a), (b) are from AB10 based on data from Middle-East Asia; two new NGA models of BA08 and CB08 based on metadata from shallow earthquakes in tectonically active regions in the World. These relations are derived for thrust faulting style and for generic soil conditions, $V_{s30} = 310$ m s^{-1}, to be comparable and to fit the conditions in this study. The observed PGAs and PGVs are mostly in the range of the empirical relationships. Generally, the ground motions obtained from simulations agree well with the observed values. At the closest distances, between 0 and 10 km, most of the simulations predict lower ground acceleration and velocity with large scatter compared to empirical relationships. Because of the distance metric R_{jb} used in this study, simulation points located on top of the fault surface projection correspond to zero distance. Maximum acceleration values range from 0.2 to 2 g, with a large of scattering at zero distance. However, the simulated peak ground parameters located both on the hangingwall and footwall show large variations at fault distances within 10 km, compared to larger distances. By now it is well known that the near fault high-frequency results are most sensitive to dynamics of the earthquake source and can not easily be modelled using a very simple description of source model and parameters (Madariaga 1983; Hartzell *et al.* 2005; Schmedes *et al.* 2010). For this reason, we assumed a constant rupture velocity along approximately 100 km of the Chelungpu Fault. This may not be correct because rupture speed is a dynamic parameter. Because this topic is beyond the objectives of this study, we did not attempt to investigate the effect of the input source rupture model regarding to fault mechanism/dimensions and the slip concentrations across the fault plane on the extent of the simulated ground shaking level.

5.7 Comparison between simulated ground motions for M_w 6.5 and 5.5 events from different regions of the world

Because the technique used here for the investigation of the scaling properties of the high-frequency parts of the ground motion is virtually identical to those used in studies conducted in a wide variety of environments (e.g. Bodin *et al.* 2004; Malagnini *et al.* 2010a), we can compare our results with those studies to reveal systematic similarities and differences with other areas. Figs 14(a), (b) show the predicted ground motions computed for moment magnitude of M_w 6.5 and 5.5 from different regions of the world using the generic rock sites by Boore & Joyner (1997), coupled with $\kappa = 0.05$ s in our case, and provide a comparison with the attenuation relationship developed by AB10.

The figure clearly describes the performance of the model developed in this study, in the range of magnitudes where the regressions were carried out. Weak-motion based predictive relationships fit quite well with the observed data from M_w 6.5 and 5.5 events in Taiwan. The predictive relationships of AB10 overestimate the PGA and PGV with compare to both our RVT-generated ground motion predictions and the observed data at lower magnitude, M_w 5.5.

The predicted decay of PGA and PGV with distance clearly indicates that Taiwanese ground motions may be similar to that observed in tectonically active regions, rather than in stable areas
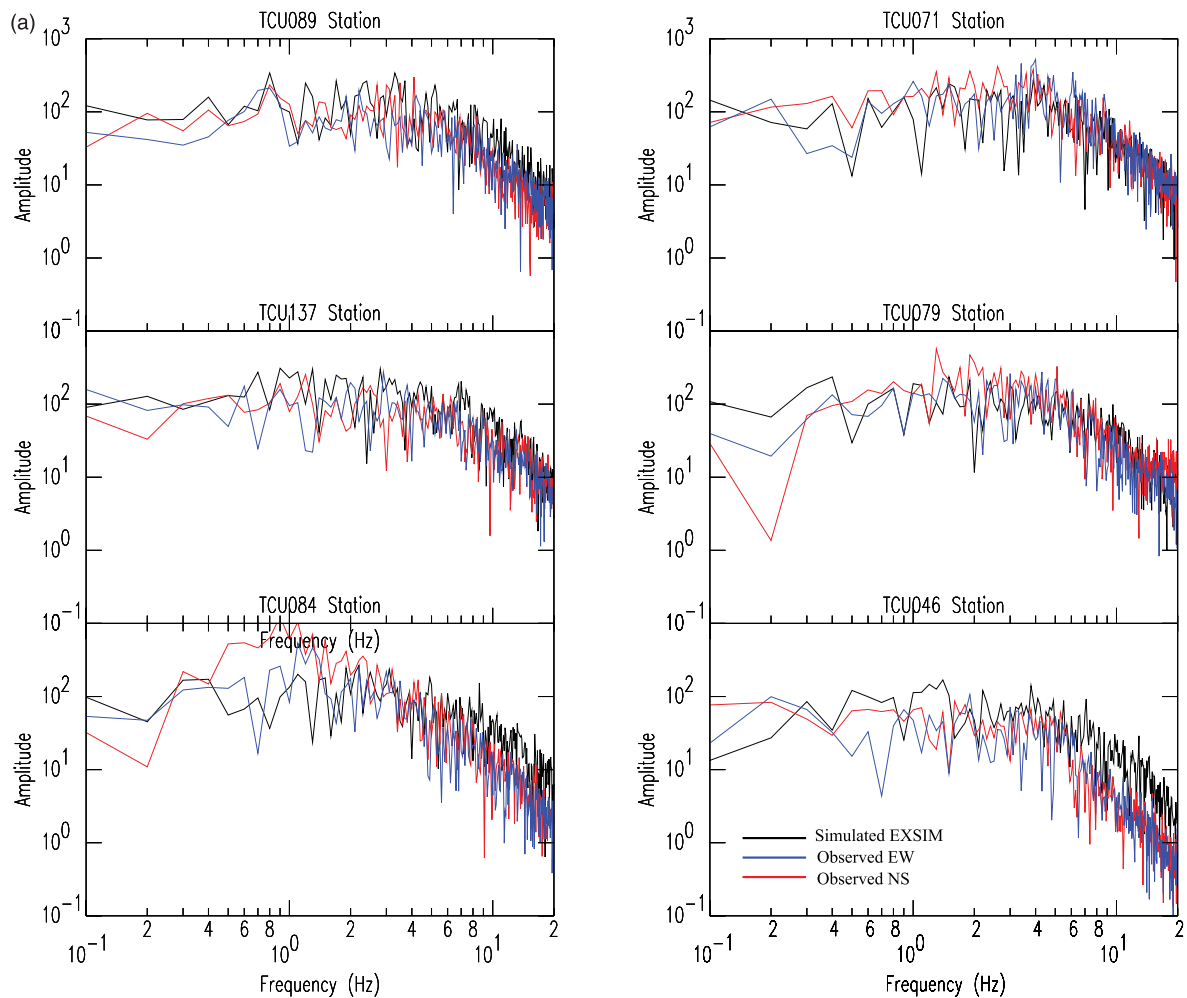
Figure 12. Comparison of observed east–west and north–south components (solid lines in red and blue colour) and simulated (solid line in black colour) Fourier amplitude spectra (cm s^{-1}) of acceleration at (a) six rock sites on the fault plane and (b) 18 rock sites at different location and distances respect to epicentre (R indicates the Joyner and Boore distance).

like the Indian Plate. The differences in the predicted peak amplitudes between regions get larger at lower magnitudes. The stronger attenuation is experienced by the high-frequency part of the spectrum because peak ground motions are carried by a dominant frequency band that is magnitude-dependent. Most of the seismic energy is radiated around the earthquake corner frequency, so that at larger magnitudes, peak ground motions are dominated by lower frequencies and are not very sensitive to crustal attenuation. Therefore, peak ground motions decay faster for the M_w 5.5 event than for the M_w 6.5 event.

Moreover, the level of ground shaking increases as the quality factor Q_o increases, and as the slope of the effective geometrical spreading function gets more gentle. The effect gets more severe for distant records. Due to the heterogeneities that are present (mainly vertically) in the crustal structure, different slopes may be presented in the predicted curves. Unfortunately, many of the existing predictive relationships (e.g. Ambraseys 1995; Sabetta & Pugliese 1996; Akkar & Bommer 2010) were obtained by forcing a body-wave geometrical spreading to a distance range where supercritical reflections at the Moho appear to be quite important. Another important parameter is the stress drop, which may cause the differences in the ground motion levels at short distances. In fact, Mayeda & Malagnini (2009) hypothesized a step-like change in the stress

parameter around M_w 5.5 using different data set from Hector Mine (CA; Mayeda *et al.* 2007), Wells (NV; Mayeda & Malagnini 2010), San Giuliano (Italy, Malagnini & Mayeda 2008), and Colfiorito (Italy, Malagnini *et al.* 2008). They found that the stress parameter does not increase systematically over the entire magnitude range; it only increases for events below M_w 5.5 (non-self-similar) and then stays constant above this magnitude (self-similar). However, Malagnini *et al.* (2010a) observed that the absolute levels of the stress drop parameters are region-dependent. For example; the stress parameter calculated from Hector Mine and Chi–Chi sequences are roughly 5 and 10 times smaller, respectively, than the two Italian, San Giuliano, Colfiorito, sequences, or for the Wells (NV) sequence.

7 CONCLUSIONS

The results of this study are carried out by using weak-motion data from the aftershocks of the 1999 September 20, $M_w = 7.6$, Chi–Chi earthquake. The average features of regional wave propagation in Taiwan were modelled as follows
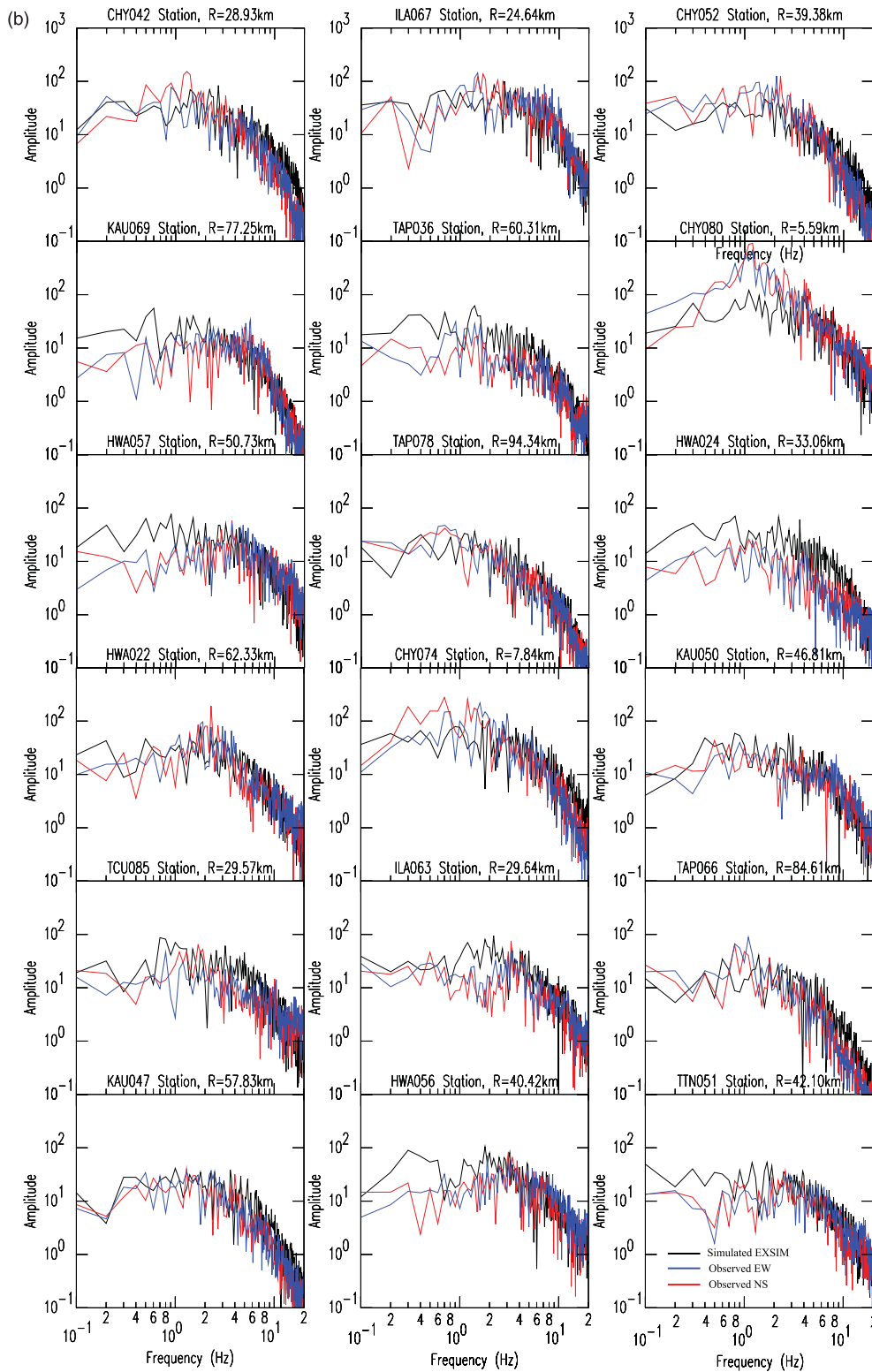
$$Q(f) = 350(f)^{0.32}$$

Figure 12. (*Continued.*)

$$g(r) = \begin{cases} r^{-1.2} & 1 < r < 10\ \text{km} \\ r^{-0.7} & 10 < r < 40\ \text{km} \\ r^{-1.0} & 40 < r < 80\ \text{km} \\ r^{-0.5} & r > 80\ \text{km}. \end{cases}$$
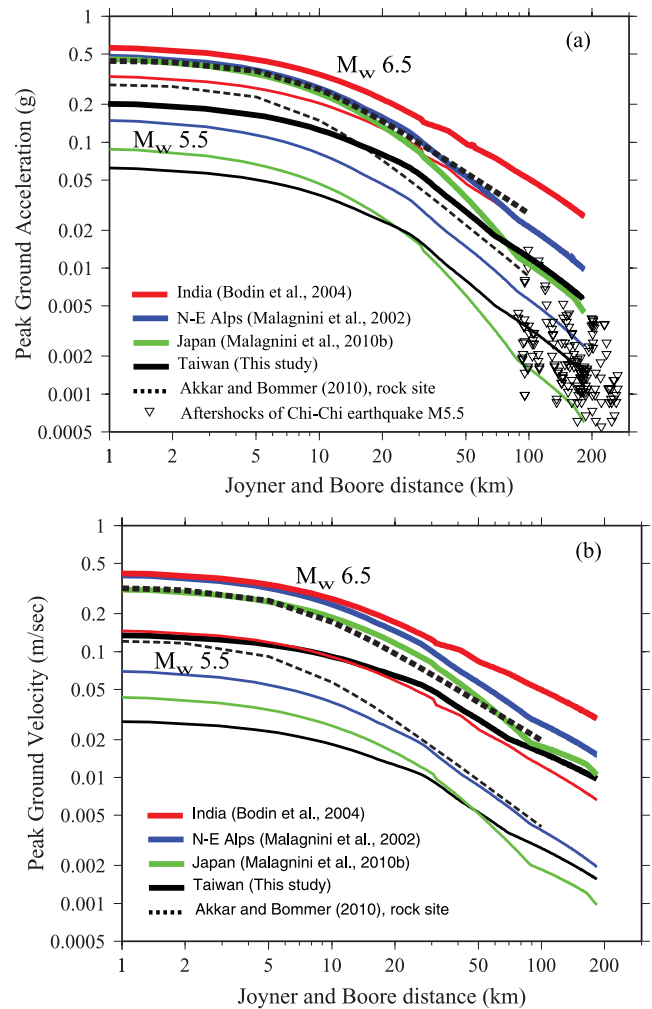
These parameters describe the averaged attenuation characteristic of the study area. Actually a trade-off exists between $g(r)$ and $Q(f)$. The inverted empirical excitation at the reference distance of 40 km was acquired from spectral values for all events (M_w 3.5–6.5). For earthquakes within the data set, up to M_w 6.5, the stress
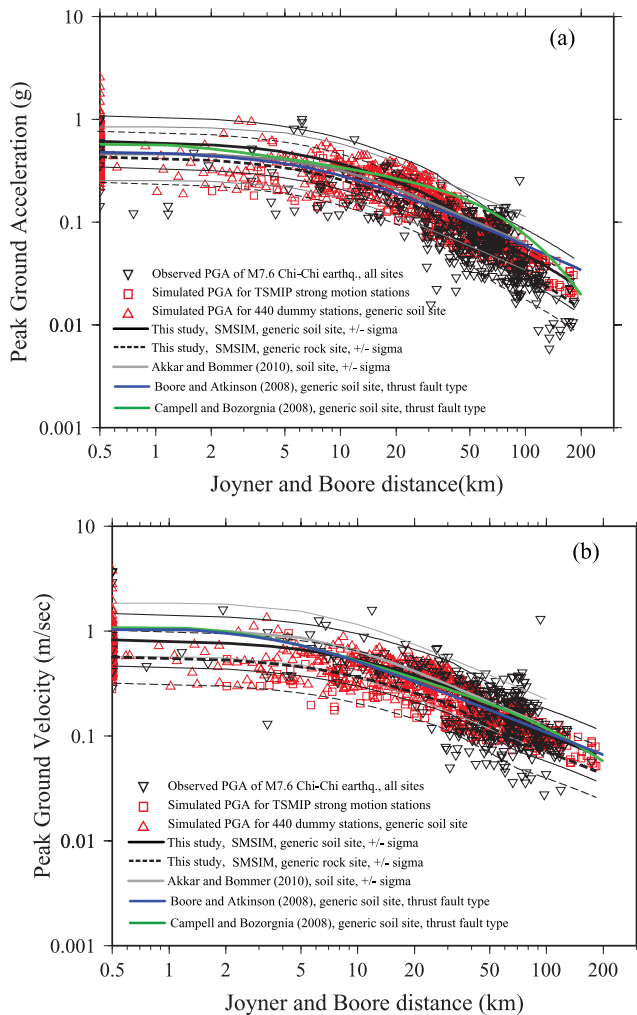
Figure 13. Comparisons between observed and simulated (a) PGA and (b) PGV. The simulation values are obtained using the EXSIM computer codes. The PGA and PGV simulated values were estimated for an earthquake of M_w 7.6 using the parameters derived in this study, and the proposed fault geometry by Ma *et al.* (2001). The grey symbols represent the observed data of the Chi–Chi earthquake (http://www.cwb.gov.tw). Predictions obtained using Akkar & Bommer (2010), Boore & Atkinson (2008) and Campbell & Bozorgnia (2008) are also shown.

Figure 14. Predictions of (a) PGA, in grams and (b) PGV, in m s^{-1} for different regions of the world: India (red lines, Bodin *et al.* 2004); N–E Alps (blue lines, Malagnini *et al.* 2002); Japan (green lines, Malagnini *et al.* 2010b); Taiwan (black lines, this study). Predictions obtained using Akkar & Bommer (2010) are also shown by dashed black lines. The thick and thin lines are the prediction of PGA and PGV for moment magnitude of 5.5 and 6.5, respectively.

parameter was calibrated by matching the empirical source terms with the Brune spectral model with a kappa parameter of 0.05 s. The frequency spectral level of excitation for the largest event in our database, with M_w 6.5, are consistent with a Brune stress drop of 8.0 MPa, as suggested by Mayeda & Malagnini (2009).

We predicted the expected ground motions for the region using a stochastic approach, to see whether our model is capable of reproducing the strong-motion data recorded during this significant and well-recorded event, which occurred in a complex tectonic setting. In the implementation of the stochastic method, the attenuation effects of the propagation path are modelled through the empirical $Q(f)$ and geometrical spreading $g(r)$. Using the regional attenuation model obtained in this study, coupled with the absolute source scaling obtained by Mayeda & Malagnini (2009), we successfully predicted the strong motions that were observed during the main shock of 1999 September 20. The large number of recorded seismograms gives us the ability to calibrate the simulations. The obtained results show a good agreement between the computations

performed in this study, the ground motion predictions derived by AB10, and the NGA models by BA08 and CB08, all based on strong-motion data. In conclusion, we demonstrated that the weak-motion based region-specific high-frequency spectral parameters can be successfully used to predict average expected ground motion amplitudes through stochastic approaches. Once the source scaling is calibrated for the region, the described approach allows predictions extrapolated to magnitudes that are not sampled in the used data set. This is really important because it will be possible to make ground motion predictions for regions where strong-motion data are lacking or for high-risk seismic areas in which just data from moderate earthquakes are available. Moreover, simulations offer a great advantage in real time estimation of peak ground motion for emergency response operations (e.g. ShakeMap®; http://earthquake.usgs.gov/earthquakes/shakemap). Our approach provides a complete solution to obtained necessary source spectra parameters on the basis of data from smaller earthquakes in the studied region and is capable of providing reliable results in the case of Taiwan region and the Chi–Chi earthquake. Of course, our

predictions generated using a stochastic approach cannot reproduce important coherent pulses that may be found in real records may be missing in our predictive results.

Our results confirm the regional dependence of ground motion, in terms of attenuation and stress parameter, in agreement with the recent studies using weak-motion waveforms recorded at local-to-regional distances (e.g. Bay *et al.* 2003; Akinci *et al.* 2006; Malagnini *et al.* 2007; Drouet *et al.* 2008; Edwards *et al.* 2008; Atkinson & Morrison 2009). We finally state that the development of global empirical ground motion predictions equations obtained combining data from regions with different attenuation characteristics for may not be always correct.

ACKNOWLEDGMENTS

REFERENCES

Aki, K., 1980. Attenuation of shear waves in the lithosphere for frequencies from 0.05 to 25 Hz, *Phys. Earth planet. Inter.,* **21,** 50–60.

Akkar, S. & Bommer, J.J., 2010, Empirical equations for the prediction of PGA, PGV, and spectral accelerations in Europe, the Mediterranean, and the Middle East. *Seism. Res. Lett.,* **81**(2), 195–206.

Akinci, A., Malagnini, L., Pino, N.A., Scognamiglio, L., Hermann, R.B. & Eyidogan, H., 2001. High-frequency ground motion in the Erzincan region. Turkey: inferences from small earthquakes, *Bull. seism. Soc. Am.,* **91,** 1446–1455.

Akinci, A., Malagnini, L., Herrmann, R.B., Gok, R. & Sorensen, M.B., 2006. Ground motion scaling in Marmara region, Turkey, *Geophys. J. Int.,* **166,** 635–651.

Akinci, A., Malagnini, L. & Sabetta, F., 2010. Characteristics of the strong ground motions from the 6 April 2009 L'Aquila earthquake, Italy, *Soil Dyn. Earthq. Eng.,* **30,** 320–335, doi:10.1016/j.soildyn.2009.12.006.

Ambraseys, N.N., 1995. The prediction of earthquake peak ground acceleration in Europe, *Earthq. Eng. Struct. Dyn.,* **24,** 467–490.

Anderson, J.G. & Hough, S.E., 1984. A model for the shape of the Fourier amplitude spectrum of acceleration at high frequencies, *Bull. seism. Soc. Am.,* **74,** 1969–1993.

Assatourians, K. & Atkinson, G., 2007. Modeling variable-stress distribution with the stochastic finite-fault technique. *Bull. seism. Soc. Am.,* **97,** 1935–1949.

Atkinson, G.M. & Boore, D.M., 2006. Earthquake ground-motion prediction equations for eastern North America, *Bull. seism. Soc. Am.,* **96,** 2181–2205.

Atkinson, G. & Morrison, M., 2009. Observations on regional variability in ground-motion amplitudes for small-to-moderate earthquakes in North America, *Bull. seism. Soc. Am.,* **99,** 2393–2409.

Atkinson, G.M. & Silva, W. 1997. An empirical study of earthquake source spectra for California earthquakes. *Bull. seism. Soc. Am.,* **87,** 97–113.

Bay, F., Fah, D., Malagnini, L. & Giardini, D., 2003. Spectral shear-wave ground motion scaling for Switzerland, *Bull. seism. Soc. Am.,* **93,** 414–429.

Beresnev, I.A. & Atkinson, G.M., 1997. Modeling finite-fault radiation from the omega**n spectrum, *Bull. seism. Soc. Am.,* **87,** 67–84.

Beresnev, I. & Atkinson, G., 1998. FINSIM: a FORTRAN program for simulating stochastic acceleration time histories from finite faults, *Seism. Res. Lett.,* **69,** 27–32.

Bodin, P., Malagnini, L. & Akinci, A., 2004. Ground motion scaling in the Kachchh basin, India, deduced from aftershocks of the 2001 M_w 7.6 Bhuj earthquake, *Bull. seism. Soc. Am.,* **94,** 1658–1669.

Boore, D.M., 1996. *SMSIM – Fortran Programs for Simulating Ground Motion from Earthquakes: Version 1.0,* U.S. Geological Survey open-file report 96–80-A, 73pp.

Boore, D.M., 2003. Simulation of ground motion using the stochastic method. *Pure appl. Geophys.,* **160,** 635–676.

Boore, D.M., 2009. Comparing stochastic point-source and finite-source ground-motion simulations: SMSIM and EXSIM, *Bull. seism. Soc. Am.,* **99,** 3202–3216.

Boore, D.M. & Atkinson, G.M., 2008. Ground-motion prediction equations for the average horizontal component of PGA, PGV, and 5%-damped PSA at spectral periods between 0.01 s and 10.0 s, *Earthq. Spectra,* **24,** 99–138.

Boore, D.M. & Joyner, W.B., 1997. Site amplification for generic rock sites, *Bull. seism. Soc. Am.,* **87,** 327–341.

Brune, J.N., 1970. Tectonic stress and the spectra of seismic shear waves from earthquakes, *J. geophys. Res.,* **75,** 4997–5009.

Brune, J.N., 1971. Correction, *J. geophys. Res.,* **76,** 5002.

Building Seismic Safety Council (BSSC), 2001. *NEHRP Recommended Provisions for Seismic Regulations for New Buildings, and Other Structures,* 2000 Edition. Part 1: Provisions, Building Seismic Safety Council for the Federal Emergency Management Agency (Report FEMA368), Washington, DC, USA.

Campbell, K.W. & Bozorgnia, Y., 2008. NGA ground motion model for the geometric mean horizontal component of PGA, PGV, PGD and 5%-damped linear elastic response spectra at periods ranging from 0.1 s to 10.0 s., *Earthq. Spectra,* **24**(1), 139–171.

Cartwright, D.E. & Longuet-Higgins, M.S., 1956. The statistical distribution of the maxima of a random function, *Proc. R. Soc. London,* **237,** 212–232.

Chang, C.H., Wu, Y.M., Shin, T.C. & Wang, C.Y., 2000. Relocation of the 1999 Chi-Chi earthquake in Taiwan, *Terr. Atm. Ocean.,* **11,** 581–590.

Chang, T.M., Wen, K.L., Furumura, T. & Chiang, H.J., 2002. Surface wave excitation in the western coastal plain of Taiwan during the 1999 Chi-Chi earthquake, *J. Chin. Inst. Eng.,* **25**(4), 461–467.

Chi, W.-C., Dreger, D. & Kaverina, A., 2001. Finite-source modeling of the 1999 Taiwan (Chi-Chi) earthquake derived from a dense strong motion network, *Bull. seism. Soc. Am.,* **91,** 1144–1157.

Chiou, B., Darragh, R., Gregor, N. & Silva, W., 2008. NGA project strong-motion database, *Earthq. Spectra,* **24,** 23–44.

Chouet, B. K. & Tsujiurs, M., 1978. Regional variation of the scaling law of earthquake source spectra, *Bull. seism. Soc. Am.,* **68,** 49–79.

Chung, J.K. & Shin, T.C., 1999. Implications of the rupture process from the displacement distribution of strong ground motions recorded during the 21 September 1999 Chi-Chi, Taiwan earthquake, *Terr. Atm. Ocean. Sci.,* **10,** 777–786.

Cotton, F., Pousse, G., Bonilla, F. & Scherbaum, F., 2008. On the discrepancy of recent European ground-motion observations and predictions from empirical models: Analysis of KiK-net accelerometric data and point-source stochastic simulations, *Bull. seism. Soc. Am.,* **98**(5), 2244–2261.

D'Amico, S., Caccamo, D., Parrillo, F., Lagana', C., Barbieri, F., 2010. The 20th September 1999 Chi-Chi earthquake (Taiwan): a case of study for its aftershock seismic sequence, *Izvestiya – Phys. Solid Earth,* **46**(4), 317–326, doi:10.1134/S106935131004004X.

Ding, Z.-Y., Yang, Y.-Q., Yao, Z.-X. & Zhang, G.-H., 2001. A thin-skinned collisional model for the Taiwan orogeny, *Tectonophysics,* **332,** 321–331.

Drouet, S., Chevrot, S., Cotton, F. & Souriau, A., 2008. Simultaneous inversion of source spectra, attenuation parameters, and site responses: application to the data of the French accelerometric network, *Bull. seism. Soc. Am.,* **98,** 198–219.

Drouet, S., Cotton, F. & Guéguen, P., 2010. v_{S30}, κ, regional attenuation and M_w from accelerograms: application to magnitude 3–5 French earthquakes, *Geophys. J. Int.,* **182,** 880–898.

Edwards, B., Rietbrock, A., Bommer, J.J. & Baptie, B., 2008. The acquisition of source, path and site effects from micro-earthquake recordings using Q tomography: Applications to the UK, *Bull. seism. Soc. Am.,* **98**(4), 1915–1935.

Hanks, T.C. & Kanamori H., 1979. A moment magnitude scale, *J. geophys. Res.,* **84**(B5), 2348–2350.

Hartzell, S., Guatteri, M., Mai, P.M., Liu, P.-C. & Fisk, M., 2005. Calculation of broadband time histories of ground motion, Part II: kinematic and

dynamic modeling using theoretical Green's functions and comparison with the 1994 Northridge earthquake, *Bull. seism. Soc. Am.,* **95,** 614–645.

Ho, C.S., 1986. A synthesis of the geological evolution of Taiwan, *Tectonophysics,* **125,** 1–16.

Huang, C.Y., *et al*. 1999. Seismic Geology of the Chi-Chi earthquake, in *Proceedings of the International Workshop on Chi-Chi Earthquake,* 1999 September 21, Taipei, Taiwan.

King, J.L. & Tucker, B.E., 1984. Observed variations of earthquake motion across a sediment-filled valley, *Bull. seism. Soc. Am.,* **74,** 137–151.

Kuo, C.H., Wen, K.L., Hsieh, H.H., Chang, T.M., Lin, C.M. & Chen, C.T., 2011. Evaluating empirical regression equations for Vs and estimating Vs30 in northeastern Taiwan, *Soil Dyn. Earth. Eng.,* **31**(3), 431–439.

Lee, C.T. & Tsai, Y.B., 2008. Mapping Vs30 in Taiwan, *Terr. Atmos. Ocean. Sci.,* **19,** 671–682.

Lee, W.H.K., Shin, T.C., Kuo, K.W., Chen, K.C. & Wu, C.F., 2001. CWB free-field strong-motion data from the 21 September Chi-Chi, Taiwan earthquake, *Bull. seism. Soc. Am.,* **91,** 1370–1376.

Liu, C.S., Huang, I.L. & Teng, L.S., 1997. Structural features of south western Taiwan, *Mar. Geol.,* **137,** 305–319.

Loh, C.-H., Lee, Z.-K., Wu, T.-C. & Peng, S.-Y., 2000. Ground motion characteristics of the Chi-Chi earthquake of 21 September 1999, *J. Earthq. Eng. Struct. Dyn,* **29,** 867–897.

Ma, K.F., Lee, C.T., Tsai, Y.B., Shin, T.-C. & Mori, J., 1999. The Chi-Chi Taiwan earthquake: large surface displacements on an inland thrust fault, *EOS, Trans. Am. geophys. Un.,* **80,** 605–611.

Ma, K.F., Mori, J., Lee, S.-J. & Yu, S.B., 2001. Spatial & temporal distribution of slip for the 1999 Chi-Chi, Taiwan, Earthquake, *Bull. seism. Soc. Am.,* **91,** 1069–1087.

Madariaga, R., 1983. High-frequency radiation from dynamic earthquake fault models, *Ann. Geophys.,* **1**(1), 17–23.

Malagnini, L. & Herrmann, R.B., 2000. Ground motion scaling in the region of the 1997 Umbria-Marche earthquake of (Italy), *Bull. seism. Soc. Am.,* **90,** 1041–1051.

Malagnini, L. & Mayeda, K., 2008. High-stress strike-slip faults in the Apennines: an example from the 2002 San Giuliano earthquakes (southern Italy), *Geophys. Res. Lett.,* **35,** L12302, doi:10.1029/2008GL034024.

Malagnini, L., Herrmann, R.B., Mercuri, A., Opice, S., Biella, G. & de Franco, R., 1997. Shear-wave velocity structure of sediments from the inversion of explosion-induced Rayleigh waves: comparison with cross-hole measurements, *Bull. seism. Soc. Am.,* **87**(6), 1413–1421.

Malagnini, L., Herrmann, R.B. & Di Bona, M., 2000a. Ground motion scaling in the Apennines (Italy), *Bull. seism. Soc. Am.,* **90,** 1062–1081.

Malagnini, L., Herrmann, R.B. & Koch, K., 2000b. Ground motion scaling in Central Europe, *Bull. seism. Soc. Am.,* **90,** 1052–1061.

Malagnini, L., Akinci, A., Herrmann, R.B., Pino, N.A. & Scognamiglio, L, 2002. Characteristics of the ground motion in Northeastern Italy, *Bull. seism. Soc. Am.,* **92,** 2186–2204.

Malagnini, L., Bodin, P., Mayeda, K. & Akinci A., 2004a. Unbiased moment-rate spectra and absolute site effects in the Kachchh Basin, India, from the analysis of the aftershocks of the 2001 Mw 7.6 Bhuj Earthquake, *Bull. seism. Soc. Am.,* **96,** 456–466.

Malagnini, L., Mayeda, K., Akinci, A. & Bragato, P.L., 2004b. Estimating absolute site effects, *Bull. seism. Soc. Am.,* **94,** 1343–1352.

Malagnini, L., Mayeda, K., Uhrhammer, R., Akinci, A. & Herrmann, R.B., 2007. A regional ground motion excitation/attenuation model for the San Francisco region, *Bull. seism. Soc. Am.,* **97**(3), 843–862, doi:10.1785/0120060101.

Malagnini, L., Scognamiglio, L., Mercuri, A., Akinci, A. & Mayeda, K., 2008. Strong evidence for non-similar earthquake source scaling in central Italy, *Geophys. Res. Lett.,* **35,** L17303, doi:10.1029/2008GL034310.

Malagnini, L., Nielsen, S., Mayeda, K. & Boschi, E., 2010a. Energy radiation from intermediate to large magnitude earthquakes: implications for dynamic fault weakening, *J. geophys. Res.,* **115,** B06319, doi:10.1029/2009JB006786.

Malagnini, L., Akinci, A., Mayeda, K., Herrmann, R.B. & Munafo', I., 2010b. Accurate predictions of strong ground motion based on weak motion data: case studies from Italy and Japan, in *Proceedings of the 2010 SSA Annual Meeting*, Portland, OR, 21–23 April 2010.

Malagnini, L., Akinci, A., Mayeda, K., Munafo, I., Herrmann, R.B. & Mercuri, A., 2011. Characterization of earthquake-induced ground motion from the L'Aquila seismic sequence of 2009, Italy, *Geophys. J. Int.,* **184,** 325–337.

Mayeda, K. & Malagnini, L., 2009. Apparent stress and corner frequency variations in the 1999 Taiwan (Chi-Chi) sequence: evidence for a step-wise increase at Mw ∼5.5, *Geophys. Res. Lett.,* **36,** L10308, doi:10.1029/2009GLD37421.

Mayeda, K. & Malagnini, L., 2010. Source radiation invariant property of local and near-regional shear-wave coda: application to source scaling for the Mw 5.9 Wells, Nevada Sequence, *Geophys. Res. Lett.,* **37,** L07306, doi:10.1029/2010GL042698.

Mayeda, K., Hofstetter, A., O'Boyle, J.L. & Walter, W.R., 2003. Stable and transportable regional magnitudes based on coda-derived moment-rate spectra, *Bull. seism. Soc. Am.,* **93,** 224–239.

Mayeda, K., Malagnini, L. & Walter, W.R., 2007. A new spectral ratio method using narrow band coda envelopes: evidence for non-selfsimilarity in the Hector Mine sequence, *Geophys. Res. Lett.,* **34,** L11303, doi:10.1029/2007GL030041.

Morasca, P., Malagnini, L., Akinci, A., Spallarossa, D. & Herrmann, R.B., 2006. Ground motion scaling in the western Alps, *J. Seismol.,* **10,** 315–333.

Motezedian, D. & Atkinson, G.M., 2005. Stochastic finite-fault modeling based on a dynamic corner frequency, *Bull. seism. Soc. Am.,* **95,** 995–1010.

Olsen, K.B., Akinci, A., Rovelli, A., Marra, F. & Malagnini, L., 2006. 3D Ground-motion estimation in Rome, Italy, *Bull. seism. Soc. Am.,* **96,** 133–146, doi:10.1785/0120030243.

Ortega, R., Herrmann, R.B. & Quintanar, L., 2003. Earthquake ground-motion scaling in Central Mexico between 0.7 and 7 Hz, *Bull. seism. Soc. Am.,* **93,** 397–413.

Roumelioti, Z. & Beresnev, I.A., 2003. Stochastic finite-fault modeling of ground motions from the 1999 Chi-Chi, Taiwan, earthquake: application to rock and soil sites with implications for nonlinear site response, *Bull. seism. Soc. Am.,* **93,** 1691–1702.

Raoof, M., Herrmann, R.B. & Malagnini, L., 1999. Attenuation and excitation of three component ground motion in Southern California, *Bull. seism. Soc. Am.,* **89,** 888–902.

Sabetta, F. & Pugliese, A., 1996, Estimation of response spectra and simulation of nonstationary earthquake ground motions, *Bull. seism. Soc. Am.,* **86**(2), 337–352.

Schmedes, J., Archuleta, R.J. & Lavallée, D., 2010. Correlation of earthquake source parameters inferred from dynamic rupture simulations, *J. geophys. Res.,* **115,** B03304, doi:10.1029/2009JB006689.

Scognamiglio, L., Malagnini, L. & Akinci, A., 2005. Ground motion scaling in eastern Sicily, Italy, *Bull. seism. Soc. Am.,* **95,** 568–578.

Sokolov, V., Yu., Loh, C.-H. & Wen, K.-L. 2002. Comparison of the Taiwan Chi-Chi earthquake strong motion data and ground motion assessment based on spectral model from smaller earthquakes in Taiwan, *Bull. seism. Soc. Am.,* **92,** 1855–1877, doi:10.1785/0120010178.

Sokolov, V., Ovcharenko, A., Loh, C.H. & Wen, K.L., 2004. Seismic hazard assessment for the Taiwan region on the basis of recent strong-motion data and prognostic zonation of future earthquakes. *Nat. Haz.,* **33,** 319–363.

Teng, L.S., 1990. Geotectonic evolution of late Cenozoin arc continent collision inTaiwan, *Tectonophysics,* **183,** 57–76.

Tsai, Y.B. & Huang, M.W., 2000. Strong ground motion characteristics of the Chi-Chi, Taiwan earthquake of September 21, 1999, *Earthq. Eng. Eng. Seism.,* **2,** 1–21.

Tsai, Y.B., Yu, T.M., Chao, H.L. & Lee, C.P., 2001. Spatial distribution and age dependence of human fatality rates from the Chi-Chi, Taiwan, earthquake of 21 September, 1999, *Bull. seism. Soc. Am.,* **91,** 1298–1309.

Yu, S.B., Chen, H.Y., Kuo, L.C., 1997. Velocity field of GPS stations in the Taiwan area, *Tectonophysics,* **274,** 41–59.

Yu, S.B., Kuo, L.C., Punongbayan, R.S. & Ramos, E.G., 1999. GPS observation of the crustal deformation in the Taiwan-Luzon region, *Geophy. Res. Lett.,* **26,** 923–926.

Wang, C.Y., Chang, C.H. & Yen, H.Y., 2000, An interpretation of the 1999 Chi-Chi earthquake in Taiwan based on the thin-skinned thrust model, *Terr. Atmos. Ocean. Sci.,* **11,** 609–630.

Wen, K.L. & Yeh, Y.-C., 2001. Nonlinear soil response during the 1999 Chi-Chi, Taiwan earthquake, *Seism. Res. Lett.,* **72,** 248.

Wen, K.L., Peng, H.Y., Tsai, Y.B. & Chen, K.C., 2001. Why 1 g was recorded at TCU129 site during the 1999 Chi-Chi, Taiwan earthquake?, *Bull. seism. Soc. Am.,* **91**(5), 1255–1266.

Wessel, P. & Smith, W.H.F., 1991. Free software helps map and display data, *EOS, Trans. Am. geophys. Un.,* **72,** 441.

Wu, Y.-M., Shin, T.-C. & Chang, C.-H., 2001. Near real-time mapping of peak ground acceleration and peak ground velocity following a strong earthquake, *Bull. seism. Soc. Am.,* **91,** 1218–1228.

Zeng, Y. & Chen, C.H., 2001. Fault rupture process of the 20 September 1999 Chi-Chi, Taiwan, earthquake, *Bull. seism. Soc. Am.,* **91,** 1088–1098.

SUPPORTING INFORMATION

Additional Supporting Information may be found in the online version of this article:

Table S1. A table of peak values (PGA, PGV and SA, at 0.33, 1.0 and 3.0), as a function of hypocentral distance and for several moment magnitudes.

Please note: Wiley-Blackwell are not responsible for the content or functionality of any supporting materials supplied by the authors. Any queries (other than missing material) should be directed to the corresponding author for the article.